J. Fluid Mech. (2005), *vol.* 531, *pp.* 11–47.
doi:10.1017/S0022112005003757 Printed in the United Kingdom

Vortex-induced vibrations of a sphere

By R. N. GOVARDHAN[1] AND C. H. K. WILLIAMSON[2]

[1]Department of Mechanical Engineering, Indian Institute of Science, Bangalore 560012, India
[2]Sibley School of Mechanical and Aerospace Engineering, Cornell University, Ithaca, NY 14853-7501, USA

(Received 7 April 2004 and in revised form 24 November 2004)

There are many studies on the vortex-induced vibrations of a cylindrical body, but almost none concerned with such vibrations for a sphere, despite the fact that tethered bodies are a common configuration. In this paper, we study the dynamics of an elastically mounted or tethered sphere in a steady flow, employing displacement, force and vorticity measurements. Within a particular range of flow speeds, where the oscillation frequency (f) is of the order of the static-body vortex shedding frequency (f_{vo}), there exist two modes of periodic large-amplitude oscillation, defined as modes I and II, separated by a transition regime exhibiting non-periodic vibration. The dominant wake structure for both modes is a chain of streamwise vortex loops on alternating sides of the wake. Further downstream, the heads of the vortex loops pinch off to form a sequence of vortex rings. We employ an analogy with the lift on an aircraft that is associated with its trailing vortex pair (of strength Γ^* and spacing b^*), and thereby compute the rate of change of impulse for the streamwise vortex pair, yielding the vortex force coefficient (C_{vortex}):

$$C_{vortex} = \frac{8}{\pi} U_v^* \, b^* (-\Gamma^*).$$

This calculation yields predicted forces in reasonable agreement with direct measurements on the sphere. This is significant because it indicates that the *principal vorticity dynamics giving rise to vortex-induced vibration for a sphere are the motions of these streamwise vortex pairs*. The Griffin plot, showing peak amplitudes as a function of the mass–damping ($m^*\zeta$), exhibits a good collapse of data, indicating a maximum response of around 0.9 diameters. Following recent studies of cylinder vortex-induced vibration, we deduce the existence of a critical mass ratio, $m^*_{crit} \approx 0.6$, below which large-amplitude vibrations are predicted to persist to infinite normalized velocities. An unexpected large-amplitude and highly periodic mode (mode III) is found at distinctly higher flow velocities where the frequency of vibration (f) is far below the frequency of vortex shedding for a static body. We find that the low-frequency streamwise vortex pairs are able to impart lift (or transverse force) to the body, yielding a positive energy transfer per cycle.

1. Introduction and preliminary work

The problem of vortex-induced vibration (VIV) of structures is important in many fields of engineering. This has led to a large number of fundamental studies that are summarized in the comprehensive reviews of Sarpkaya (1979), Griffin & Ramberg (1982), Bearman (1984), Parkinson (1989) and Williamson & Govardhan (2004) and the books by Blevins (1990), Naudascher & Rockwell (1994), Sumer & Fredsoe (1997) and Anagnostopoulos (2002). Most of these studies have been on cylindrical structures,

and prior to some preliminary work (Williamson & Govardhan 1997; Govardhan & Williamson 1997; Jauvtis, Govardhan & Williamson 2001) there is almost no reported work on vortex-induced vibrations of a sphere despite its practical significance. Some practical examples include tethered bodies like marine buoys, underwater mines, tethered balloons in the atmosphere, and towed objects behind ships.

In the present work, we are interested in the case of an elastically mounted sphere in a steady uniform flow, which is perhaps one of the most basic fluid–structure interaction problems that one can imagine. We shall consider both the case where the sphere is free to move only along the transverse (y) direction to the flow, and also the case where the sphere is tethered and is thus free to move in both the streamwise (x) and transverse (y) directions. For the cylinder, the transverse (y-only) case has been extensively studied, while there are very few recent studies on the more practical situation where the cylinder is free to move in both transverse and streamwise directions (Moe & Wu 1990; Sarpkaya 1995; Jeon & Gharib 2001; Jauvtis & Williamson 2003, 2004). It should be noted here that recently Provansal, Schouveiler & Leweke (2004) have reported on preliminary experiments on the dynamics of a neutrally buoyant tethered sphere at low Reynolds numbers ($Re = 600 - 800$). For this configuration, where the tether is parallel to the flow, they find periodic trajectories, such as elliptic orbits in the cross-section normal to the flow. The range of Reynolds numbers for the present investigation is from $Re = 2000$ to $Re = 12\,000$. Although not directly relevant to the present problem, it should also be mentioned that there have been some previous investigations of the dynamics of a tethered sphere in surface waves (Harleman & Shapiro 1961; Shi-Igai & Kono 1969; Ogihara 1980; Vethamony, Chandramohan & Sastry 1992; Carpenter, Leonard & Yim 1995).

In the conceptually simple case of the elastically mounted sphere in a steady flow, we seek to understand the following fundamental questions in the present work:

What modes of response exist for an elastically mounted sphere?

What are the principal vortex dynamics that can give rise to vortex-induced vibration of a three-dimensional body such as a sphere?

How does the peak amplitude response vary with mass and damping?

What is the effect of mass ratio on the amplitude and frequency response?

We shall briefly introduce an equation of motion to represent the oscillations of the sphere in the transverse y-direction (perpendicular to the free stream), in the manner of the equation generally used in the cylinder VIV case, as

$$m\ddot{y} + c\dot{y} + ky = F_y, \tag{1.1}$$

where m = total oscillating structural mass (i.e. not including fluid added mass); c = structural damping; k = spring constant; F_y = fluid force in the transverse direction. When the body oscillation frequency is synchronized with the periodic vortex wake mode, it is often found in VIV problems that the response displacement $y(t)$ and the force $F_y(t)$ are represented well by

$$y(t) = A\sin(\omega t), \tag{1.2}$$

$$F_y(t) = F_o\sin(\omega t + \phi), \tag{1.3}$$

where $\omega = 2\pi f$; f = transverse oscillation frequency. The phase angle ϕ, between the fluid force and the body displacement, is crucial in determining the energy transfer from the fluid to the body motion, and hence in influencing the amplitude of oscillation, as pointed out clearly in previous papers on cylinder VIV. We select a set of relevant non-dimensional parameters in table 1.

Mass ratio	m^*	$\dfrac{m}{\pi\rho D^3/6}$
Damping ratio	ζ	$\dfrac{c}{2\sqrt{k(m+m_A)}}$
Normalized velocity	U^*	$\dfrac{U}{f_N D}$
Amplitude ratios	$A_x^* \quad A_y^*$	$\dfrac{A_x}{D} \quad \dfrac{A_y}{D}$
Transverse frequency ratio	f^*	$\dfrac{f}{f_N}$
Transverse force coefficient	C_Y	$\dfrac{F}{\frac{1}{2}\rho U^2(\pi D^2/4)}$
Reynolds number	Re	$\dfrac{\rho U D}{\mu}$
Strouhal number	S	$\dfrac{f_{vo} D}{U}$

TABLE 1. Non-dimensional groups. Streamwise direction is along the x-axis, and the y-direction is transverse to the flow. The added mass, m_A, is given by $m_A = C_A m_d$, where m_d is the displaced fluid mass and C_A is the potential added mass coefficient. ($C_A = 0.5$ for a sphere). In the above groups, $f_N =$ mechanical natural frequency in the medium, $D =$ sphere diameter, $\rho =$ fluid density, $U =$ free-stream velocity, $\mu =$ viscosity, $f_{vo} =$ non-oscillating body vortex shedding frequency. It is straightforward to define a damping ratio based on critical damping in vacuo, by multiplying ζ by the factor $[(m^* + C_A)/m^*]^{1/2}$.

The response amplitude and frequency may be derived in a straightforward manner from equations (1.1)–(1.3), and are formulated here, along the lines of Khalak & Williamson (1999) for a cylinder, as follows:

$$A_y^* = \frac{3}{32\pi^2}\frac{C_Y \sin\phi}{(m^* + C_A)\zeta}\left(\frac{U^*}{f^*}\right)^2 f^*, \tag{1.4}$$

$$f^* = \sqrt{\frac{(m^* + C_A)}{(m^* + C_{EA})}}, \tag{1.5}$$

where C_A is the potential flow added mass coefficient ($C_A = 0.5$ for a sphere), and C_{EA} is an 'effective' added mass coefficient that includes an apparent effect due to the total transverse fluid force in phase with the body acceleration ($C_Y \cos\phi$):

$$C_{EA} = \frac{3}{16\pi^2 A_y^*}\left(\frac{U^*}{f^*}\right)^2 C_Y \cos\phi. \tag{1.6}$$

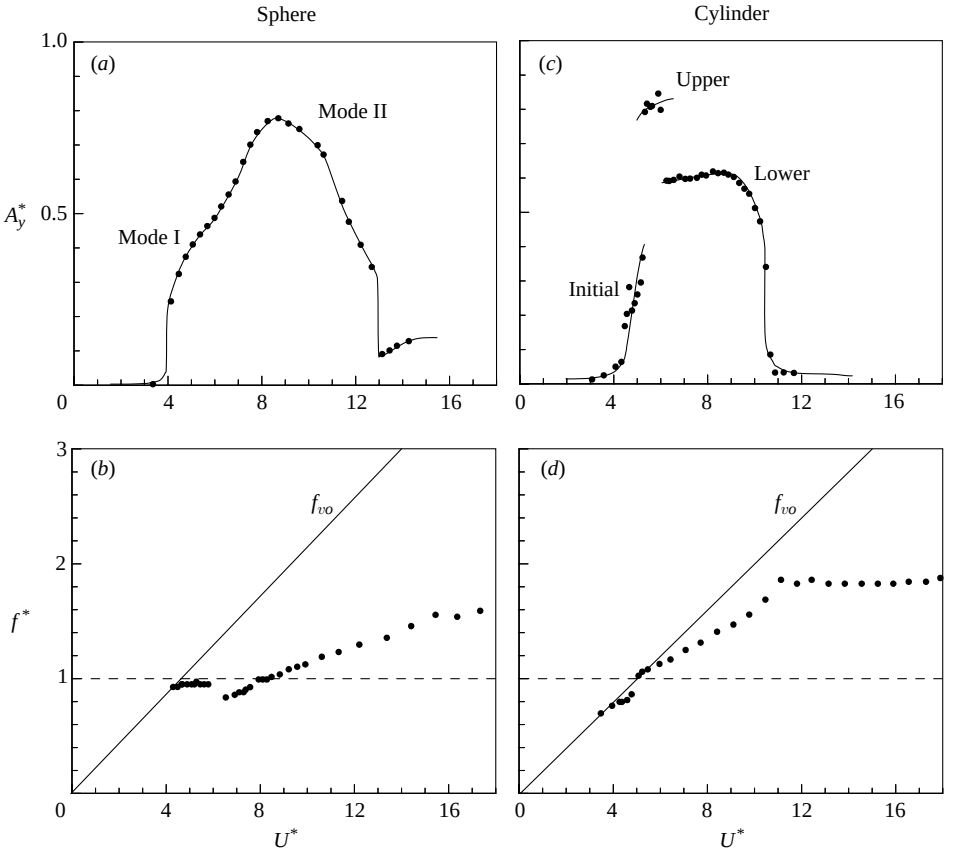

FIGURE 1. Comparison of typical VIV response for a sphere and a cylinder. In both cases, we observe similar multiple response modes, as well as similar characteristics whereby the vibration frequency rises distinctly higher than the system natural frequency ($f^* > 1$). In (a) and (b), we show sphere amplitude (A^*) and frequency (f^*) response (for somewhat different experimental conditions: (a) $m^* = 2.83$; (b) $m^* = 0.76$, where $\zeta = 0.008$ in both cases). In (c) and (d), we show cylinder VIV response ((c) $m^* = 8.63$, $\zeta = 0.0015$; (d) $m^* = 1.19$, $\zeta = 0.005$), from Govardhan & Williamson (2000). The line for f_{vo} indicates the static-body shedding frequency. Reynolds number, $Re \sim 3500$ for peak response conditions, in all cases.

In this work, we determine f_N in water by actually measuring f_N in air (close to its value in vacuo), and thereafter multiply this value by the factor $[m^*/(m^* + C_A)]^{1/2}$ to deduce f_{Nwater}. (It is simple therefore to determine f^*_{vac} accurately by multiplying our f^* by this factor, if so desired).

The first and most obvious question that one might ask regarding the vortex-induced vibrations of a sphere is: *Does an elastically mounted sphere vibrate in a steady flow?* The answer to this most basic question was apparently not made clear prior to some preliminary work reported in Williamson & Govardhan (1997), where it was shown that the elastically mounted sphere does indeed oscillate vigorously at large transverse amplitudes of the order of a diameter, over a range of flow speeds. (The fact that tethered bodies vibrate in a flow was probably well known within offshore engineering companies, as well as to children with balloons, rather than in the general literature). Typical transverse vibration response (A^*_y) can be seen in figure 1, compared with typical cylinder response. It should be noted that, although the tethered sphere

response was obtained for a body free to move in both the streamwise (x) and the transverse (y) directions, similar responses are also obtained for the spheres constrained to move transverse to the flow direction, as will be shown in the present work.

Similar broad characteristics of the response amplitude and frequency are found for the sphere and cylinder VIV cases in figure 1. The amplitude response, for the cylinder, indicates three distinct response branches, namely 'Initial', 'Upper' and 'Lower' branches. These three modes are separated by two mode jumps, at the Initial $\leftrightarrow$ Upper, and Upper $\leftrightarrow$ Lower mode transition. Govardhan & Williamson (2000) showed that there is a phase jump corresponding to each of the mode transitions; the Upper $\leftrightarrow$ Lower transition is associated with a jump in the conventionally used 'total phase' (between total transverse force and displacement), while the Initial $\leftrightarrow$ Upper mode jump is associated with a jump in 'vortex phase' (between the 'vortex force' and the displacement). It was also shown using simultaneous force and digital particle image velocimetry (DPIV) measurements, that the switch in the timing of vortex shedding is linked to a jump in 'vortex phase' (at the first discontinuity), and not to the jump in 'total phase'. This raises the question: *Is there a change in the timing of vortex formation for the elastically mounted sphere?* In the present work, we shall show using DPIV measurements in the sphere wake coupled with direct force measurements that such a change in the timing of vortex shedding does occur for the elastically mounted sphere, although it is not necessarily as sharp as for the cylinder. Further, we shall use this change in the timing of vortex formation to demarcate two modes of periodic response, namely Mode I and Mode II, within the response plot for the sphere in figure 1.

One might note that the character of the cylinder response, as shown in figure 1, is reasonably unaffected by a variation of Reynolds number, at least over the range 2000–30 000 (see Williamson & Govardhan 2004), although the peak amplitudes of the upper branch are found to increase with Re. (The fact that the general characteristics of the response for both the sphere and cylinder is quite unaffected by a variation of Re, in investigations to date, is apparently not the case when a cylinder is 'tethered' at both ends of the span, where Carberry, Ryan & Sheridan (2003*b*) find distinct changes in response and vortex modes as flow speed and Re change.)

In the case of the circular cylinder, the forced vibration experiments by Williamson & Roshko (1988) over a wide range of normalized flow speeds and amplitudes, showed a number of different vortex formation modes, which were defined, for example, as '2S' indicating 2 Single vortices formed per cycle and '2P' meaning 2 Pairs of vortices formed per cycle. For a transversely oscillating sphere, the only related work looking at such a synchronized wake structure (to the best of our knowledge) is the recent study of Brücker (1999), on the wake structure behind a bubble rising through a fluid, in a zig-zag path. Using careful DPIV measurements of the streamwise vorticity, he was able to infer the existence of hairpin vortices of the type seen for a stationary sphere, as observed for example by Ormières & Provansal (1999). In the stationary sphere case, it is well known that there exist two wake transitions as Re is increased. The first transition at $Re \approx 200$, results in the wake losing its axisymmetry, and forming two steady streamwise vortex trails. The formation of trailing vortex pairs, aligned with the flow, in the wake of an axisymmetric body, was mentioned 75 years ago in the original work of Stanton & Marshall (1930), who clearly observed such a wake downstream of a circular disk normal to the flow. The other transition at $Re \approx 280$ for a sphere, results in the wake becoming unsteady with periodic shedding of vortex loops, often referred to as hairpin vortices. For Reynolds numbers above the second transition, experimental visualizations from Sakamoto & Haniu (1990) and

more recently the striking visualizations of Leweke *et al.* (1999), show that all the shed hairpin vortices are one-sided, although the study by Johnson & Patel (1999) indicates that there might also exist small induced hairpin vortices of opposite sign in between the one-sided structures. On the other hand at $Re > 800$, Sakamoto & Haniu (1990) indicate, from dye visualizations, that the sphere wake is a two-sided chain of shed hairpin vortices of alternate sign, of the type also clearly visualized in Perry, Lim & Chong (1980) in the case of a coflowing jet or wake. In the present study at Reynolds number in the range 2000–12 000, we will find the principal vorticity of the vibrating sphere wake to comprise a two-sided chain of vortex loops, with the appearance of alternating-sign vortex rings further downstream. The sides of the vortex loops consist of 'streamwise vortex pairs', where the vortex axes align approximately parallel with the free stream (in the manner of aircraft wing tip vortices). In this work, such streamwise vortex pairs should not be confused with the clearly different vortex pairs formed by a vibrating cylinder, where, in that case, the vortex axes are principally normal to the free stream.

A fundamental question regarding such an elastically mounted system, is how the peak amplitude response will vary as a function of mass and damping $\{m^*, \zeta\}$? Much recent discussion on this point for an elastically mounted cylinder is reviewed in Williamson & Govardhan (2004). The effective use of a 'Griffin plot', whereby the peak response amplitude (A^*_{max}) for the cylinder has been plotted versus a combined mass–damping parameter, $(m^* + C_A)\zeta$, will yield a good collapse of such data in the present case for the sphere.

The effect of the mass of the body on the amplitude and frequency response of a cylinder (at fixed mass–damping) has received a lot of attention recently. In the classical cylinder experiments in air, like Feng (1968), the mass ratios were very high, $m^* \sim 100$, and the corresponding oscillation frequency was very close to f_N, such that $f^* = f/f_N \approx 1$, at which point the wake formation frequency also matches the body vibration frequency, and we have synchronization. However, at the low mass ratios typically found for a structure vibrating in water where $m^* = O(10)$, Moe & Wu (1990), Khalak & Williamson (1997), Gharib *et al.* (1998) and Govardhan & Williamson (2000) observe a marked departure of f^* from unity during synchronization, as may be seen from the frequency response for a cylinder in figure 1. A similar departure is also seen for the elastically mounted sphere at low m^*, as shown by the typical response in figure 1. This deviation of f^* is not unexpected, based on the discussion in the reviews of Bearman (1984) and Williamson & Govardhan (2004).

The recent cylinder VIV experiments of Khalak & Williamson (1996, 1997) at low mass ratio (where the mass–damping ($m^*\zeta$) was maintained at a very low value) show a significant increase in the regime of synchronization (the extent of U^* over which there are significant vibrations) as m^* is reduced. However, they found that the data sets collapse very well when replotted versus the parameter $(U^*/f^*)S$, which is equivalent to (f_{vo}/f) (or the inverse of the ratio of actual body oscillating frequency to the fixed-body shedding frequency). With the above parameter, a good correspondence was also found between the vortex wake modes of the free response branches and the vortex mode regimes deduced from forced vibration in the Williamson & Roshko (1988) map of modes. In the present work with the sphere, we shall explore regimes of vibration in such a plane $\{(U^*/f^*)S,\ A^*_y\}$.

Recent experiments for a cylinder (Govardhan & Williamson 2000, 2002) indicate that the synchronization regime can be extremely large for low m^*. In fact, it was shown that there exists a critical mass ratio (m^*_{crit}), below which the synchronization regime will continue indefinitely to infinite U^*. Under these conditions, large-amplitude

vibrations will persist up to infinite velocities, while the frequency (f^*) also increases indefinitely. The numerical value of the critical mass ratio for the circular cylinder, at low mass–damping, was determined to be 0.54. In our preliminary experiments on the tethered sphere in Williamson & Govardhan (1997), for small mass ($m^* < 1$), we were unable to reach the end of the synchronization regime for the highest velocities possible in our water channel. This suggests that our mass ratios could have been close to or below a critical value. Based on the present measurements, we shall evaluate the critical mass for a sphere in vortex-induced vibration.

The synchronization regime discussed so far has been for flow speeds where the body oscillation frequency (f) is close to the static body vortex shedding frequency (f_{vo}), so that $(U^*/f^*)S = (f_{vo}/f) \sim 1$. At high normalized velocities outside this 'fundamental synchronization regime', the cylinder does not show any significant response, as may be seen from figure 2(*c*), taken from our own cylinder VIV experiments. However, in the case of the sphere, large periodic oscillations are seen at high normalized velocities, as discovered by Jauvtis *et al.* (2001), and shown in figure 2(*a*). Although it seems as though the sphere response terminates at $(U^*/f^*)S \approx 2.2$, a new and quite surprising mode of oscillation appears when $(U^*/f^*)S > 3.0$, which we refer to as mode III. The body oscillations in this mode are highly periodic, as indicated by the example time trace in figure 3. This regime can continue to rather large normalized velocities, $(U^*/f^*)\mathrm{S} \sim 8$. This would imply that a large number of vortex structures are shed per oscillation cycle (based on observations of the static sphere wake), and raises the important question of how the fluid is able to transfer energy through the vortical wake to the body, for these mode III oscillations to exist. In the present work, we shall show that there exist periodic streamwise vortex pairs which force the structure to vibrate.

It should be noted that the mode II and mode III regimes are not always separated by a desynchronized region. When the sphere is constrained to move only in the y-direction, with low mass–damping, the mode II and mode III regimes are joined, as may be seen from figure 2(*b*). However, a distinct change in the slope of the amplitude response curve still distinguishes the two regimes. For the sphere that is free to move in both the transverse and streamwise directions, this was not seen to occur, and there was always a desynchronized regime between modes II and III.

Following a description of the experimental details in the next section (§ 2), we shall present the effect of a very large variation in mass–damping and mass ratio on the response within the fundamental synchronization regime, in § 3. We shall look at direct force measurements on the elastically mounted sphere in § 4. The wake structure corresponding to the two modes will be discussed in § 5 utilizing flow visualization and DPIV vorticity measurements in two perpendicular planes. Using the measured vorticity and the concept of vorticity impulse applied to the streamwise vortex pairs (in analogy with the trailing vortex pairs behind an aircraft), we shall predict the unsteady lift force on the body in § 6. One may deduce from the agreement with direct force measurements, that it is the dynamics of such streamwise vorticity which gives rise to vibrations of a sphere. The wake vortex structures that enable the unexpected existence of the periodic mode III oscillations at high normalized velocities will be discussed in § 7. In § 8, we investigate the effect of mass ratio on the response dynamics, evaluating a critical mass of $m^*_{crit} \approx 0.6$ for the sphere. Finally, we present conclusions in § 9.

2. Experimental details

The experiments with the sphere constrained to move transverse (y) to the flow direction, were performed with the hydroelastic facility described in detail in

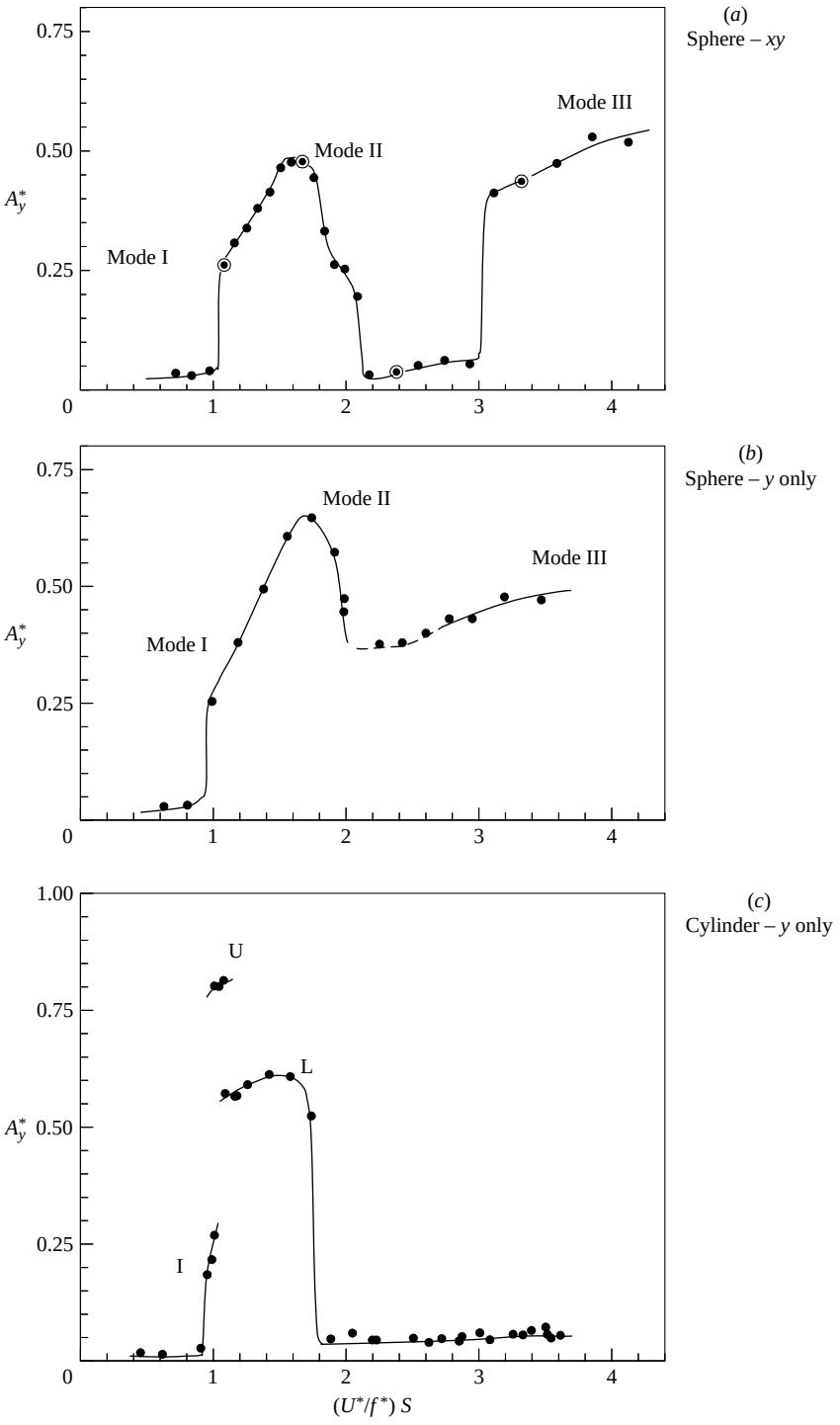

FIGURE 2. Response amplitude plots for different VIV systems over a wide range of normalized velocities, $(U^*/f^*)S$. The mode III response for the elastically mounted or tethered sphere in (*a*) and (*b*) is clearly not evident in the cylinder VIV system in (*c*). Mass and damping values are: (*a*) $m^* = 11.7$, $\zeta = 0.0025$, (*b*) $m^* = 53.7$, $\zeta = 0.017$, (*c*) $m^* = 27.5$, $\zeta = 0.0054$. *Re* at maximum A_y^* is close to 3000 for all cases.

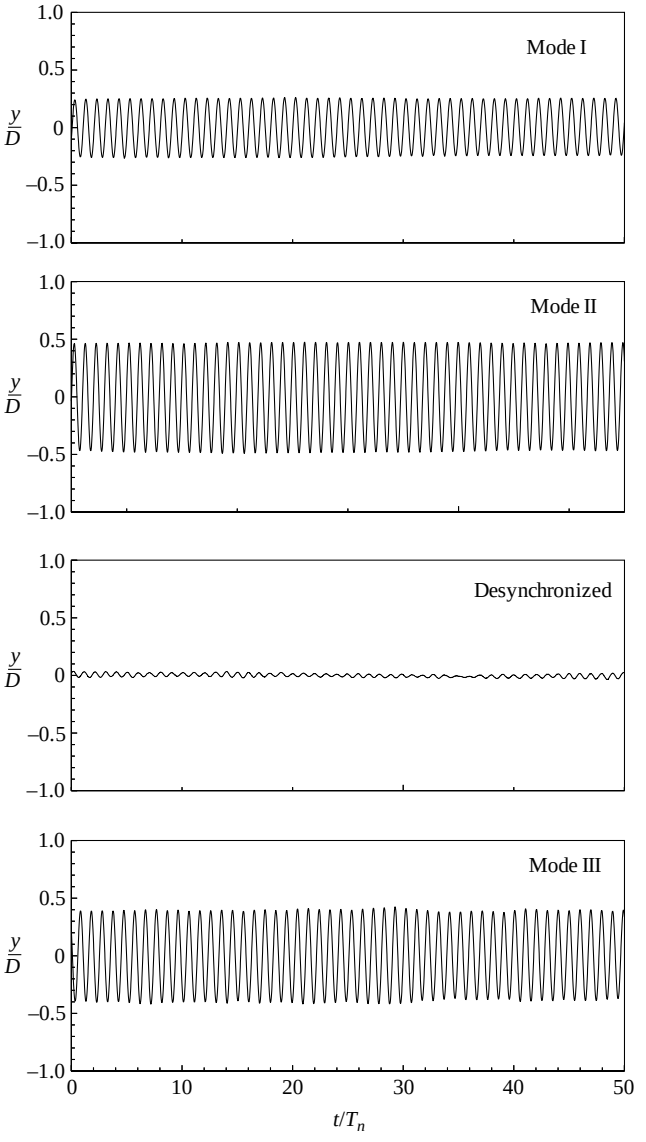

FIGURE 3. Highly periodic vibration is observed for modes I, II and III for the tethered sphere. These time traces, along with the desynchronized response case, correspond to the ⊙ symbols in figure 2(*a*).

Khalak & Williamson (1999), in conjunction with the Cornell-ONR Water Channel. The hydroelastic facility comprises air-bearings mounted above the channel test section, which allows a sphere in the fluid, supported by a vertical thin rod, to move transverse to the free stream, as shown in figure 4(*a*). The fluctuating lift force acting on the sphere was measured by a force balance utilizing LVDTs (linear variable displacement transducers), while the body displacement was measured using a non-contact (magnetostrictive) position transducer. The turbulence level in the test section of the water channel was less than 0.9%, in the 15 in. × 20 in. (0.381 m × 0.508 m)

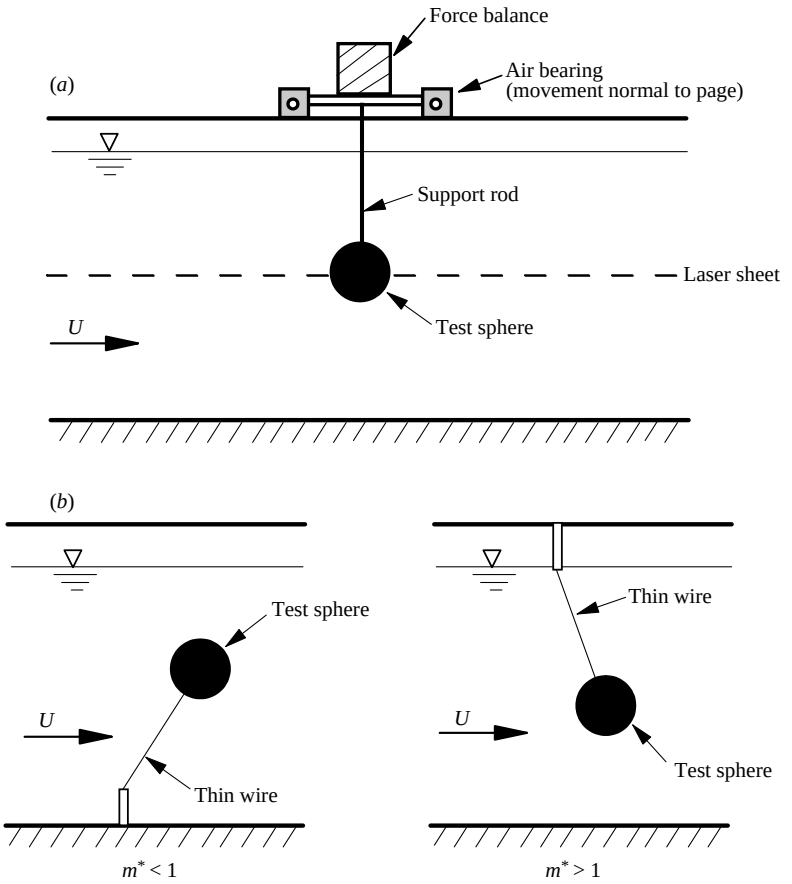

FIGURE 4. Schematic of the experimental arrangement for the elastically mounted sphere, seen in side-view. (*a*) Hydroelastic sphere constrained to move only transverse to the free stream in a direction normal to the page (y-only). (*b*) Tethered sphere free to move in both the transverse and streamwise directions (xy-motion), for buoyant spheres ($m^* < 1$) and for heavy spheres ($m^* > 1$).

cross-section, over the range of free-stream velocities U ($0.04 - 0.32\,\mathrm{m\,s^{-1}}$) used in this study.

The other set of experiments employed a tethered sphere, which allowed both streamwise (x) and transverse (y) motions. For 'heavy' spheres with $m^* > 1$ the tether was attached to the top of the test section, as shown in figure 4(*b*), while for 'light' buoyant spheres with $m^* < 1$, the point of tether attachment was at the base of the test section. For these tethered spheres, displacements of the body were obtained using an Optron optical bi-axial displacement transducer. These tethered sphere experiments were performed both in the Cornell-ONR water channel (for low m^*), and in an open-circuit suction wind tunnel (for very high m^*). The turbulence intensity in the $30.5\,\mathrm{cm} \times 30.5\,\mathrm{cm}$ test section of the wind tunnel was within 0.1%. The natural frequency (f_N) of these tethered systems depends on both the net buoyancy or weight of the sphere, and the drag on the body, as discussed in Williamson & Govardhan (1997). In the present experiments, the natural frequency (f_N) was calculated using relations from Williamson & Govardhan (1997), although as discussed in that paper, in most cases the drag force may be neglected, and f_N is given by the approximate

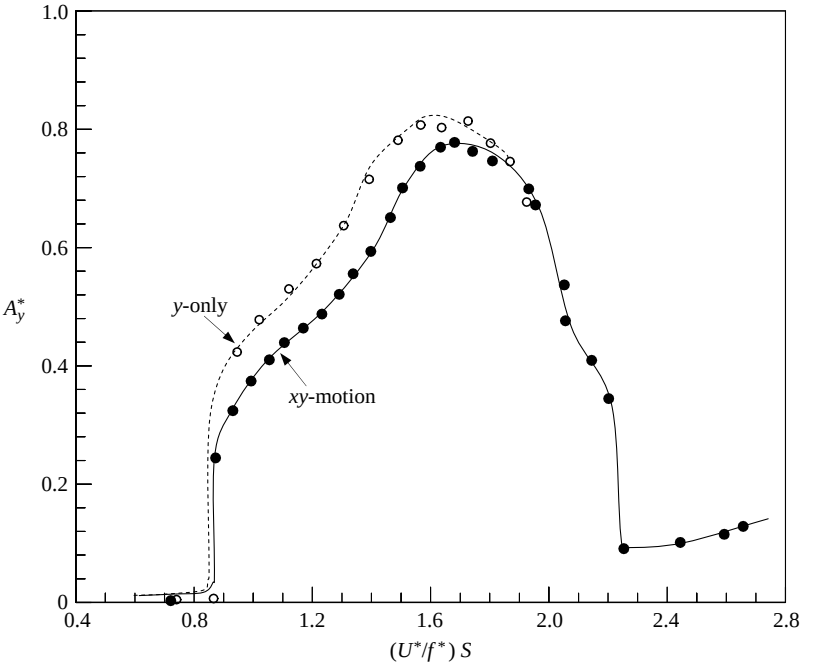

FIGURE 5. Comparison of amplitude response for a sphere free to move only in the transverse direction (y-only), and for a tethered sphere that is free to move in both the transverse and streamwise directions (xy-motion). Mass-damping parameter $(m^* + C_A)\zeta$ is approximately 0.03 in both cases. Re at maximum A_y^* is 3,500 for xy-motion, and 12 000 for y-only case. ●, xy-motion sphere ($m^* = 2.8$); ○, y-only sphere ($m^* = 7.0$).

relation:

$$\frac{f_N D}{U} \approx \left(\frac{1}{2\pi}\right) \frac{1}{Fr\,\sqrt{(L/D)}} \sqrt{\frac{1 - m^*}{m^* + C_A}}, \tag{2.1}$$

where $Fr = U/\sqrt{gD}$ is the Froude number, and L is the tether length. On a related note, the structural damping of these tethered systems was estimated from the energy dissipated in one cycle, due to the drag acting on the tether line, as it moves through the fluid. Another aspect of such tethered bodies is the extent to which they lean over due to body drag, and as one might expect this 'tether angle' increases with flow speed, as shown by measurements in Williamson & Govardhan (1997). In the experiments reported here, this tether angle had a maximum value of 25° from the vertical, at the highest flow speeds, with typical angles of around 12° at maximum transverse response (for flow speeds yielding $(U^*/f^*)S = 1.8$ in figure 8). The principal body oscillations are in the transverse y-direction. Vertical oscillations in the z-direction amount to less than 5% of those in the transverse direction. It should also be mentioned here that the body response for the tethered sphere (xy motion) and hydroelastic sphere (y-only) compared well for similar mass–damping parameter, as shown in the example of figure 5.

Spheres of diameters ranging from 0.0254 m to 0.0817 m, made of plastic and aluminium, were used in this study. The diameter of the supporting rod used with the air-bearing system was typically about 30 times smaller than the diameter of the test sphere, while for the tethered sphere experiments, the diameter of the tether wire used was typically about 200 times smaller than the diameter of the test sphere.

The velocity field in two perpendicular planes within the sphere wake was measured using digital particle image velocimetry (DPIV). For this purpose, the flow was seeded with 14-micron silver-coated glass spheres, which were illuminated by a sheet of laser light from a 5 W Argon ion laser. Our implementation of the technique is essentially as described in detail in Govardhan & Williamson (2000). We used a two-step windowing process (with window shifting) to obtain particle displacements between image pairs to deduce the velocity field. In all cases, 64×64 pixel interrogation boxes were used for the first correlation followed by 32×32 pixel boxes for the second correlation. The number of particles in a 32×32 pixel window was approximately of the order of 15, high enough to give strong correlations, although the volume fraction of the tracer particles was very small, of the order of 2×10^{-6}. A box overlap of 50% was used in the second correlation, which resulted in a set of 3600 vectors (60×60) for a typical velocity field.

For the spatio-temporal reconstruction of the sphere wake, 16 sets of streamwise vorticity fields, each phase-averaged over 10 cycles, were used. Circulation strengths of the streamwise vortex pairs and their location were measured from the individual vorticity plots, and three-dimensional spatio-temporal views generated with a simple spline fit for the strength and location of the vortex pairs. A convection velocity U (equal to the free-stream velocity) has been used for the purpose of 3D image construction, so that time t may be converted into streamwise location using $x = Ut$.

All the obtained images, and hence the DPIV velocity fields, were phase referenced with respect to the position signal. This allowed possible phase averaging (over 10 cycles) of the velocity fields, along the lines of Gu, Chyu & Rockwell (1994). This is useful at the moderate Reynolds numbers of interest ($Re \sim 2000$ to 12 000) in the present study, to obtain a clear picture of the synchronized large-scale wake vortex structures, without the presence of weak smaller scale vortical structures. There is a thickening (around 10%) of the separating shear layers close to the body from the averaging process, and the layers seem somewhat thick. However, the resulting vorticity images are comparable with the photographic PIV measurements of Carberry *et al.* (2003*a*) for a cylinder wake at similar Reynolds numbers. Throughout this paper, we have defined the normalized transverse amplitude response (A_y^*), as $A_y^* = \sqrt{2}\,(y_{rms}/D)$, which for purely sinusoidal oscillations, is simply the amplitude of motion.

The origin of the coordinate system is fixed at the centre of the sphere, at zero displacement. The x-axis is measured downstream, the y-axis is horizontal and perpendicular to the flow direction, and the z-axis is vertical. We describe motions as 'streamwise' if they are roughly parallel to the free stream (x-direction), and 'transverse' when they are roughly parallel to the y-direction. Since the dominant dynamics in all the present experiments are transverse to the flow, we note later that there is obviously a preferred orientation of the streamwise vortex pairs in the wake, which is naturally induced by these vibrations. The calculated transverse force in § 6 is also termed as a 'lift' force (in the y-direction), in analogy with aircraft trailing wake vortices.

3. Response measurements

As described in the Introduction, the elastically mounted sphere shows two modes of response within the fundamental synchronization region. In this section, we shall focus our attention on this principal regime, and investigate the effect of a very large variation in the mass–damping parameter $[(m^* + C_A)\zeta]$, and mass ratio (m^*), on the response. The mass–damping parameter will be varied over three orders in magnitude from about 0.001 to 1. The mass ratio will be varied over nearly four orders of

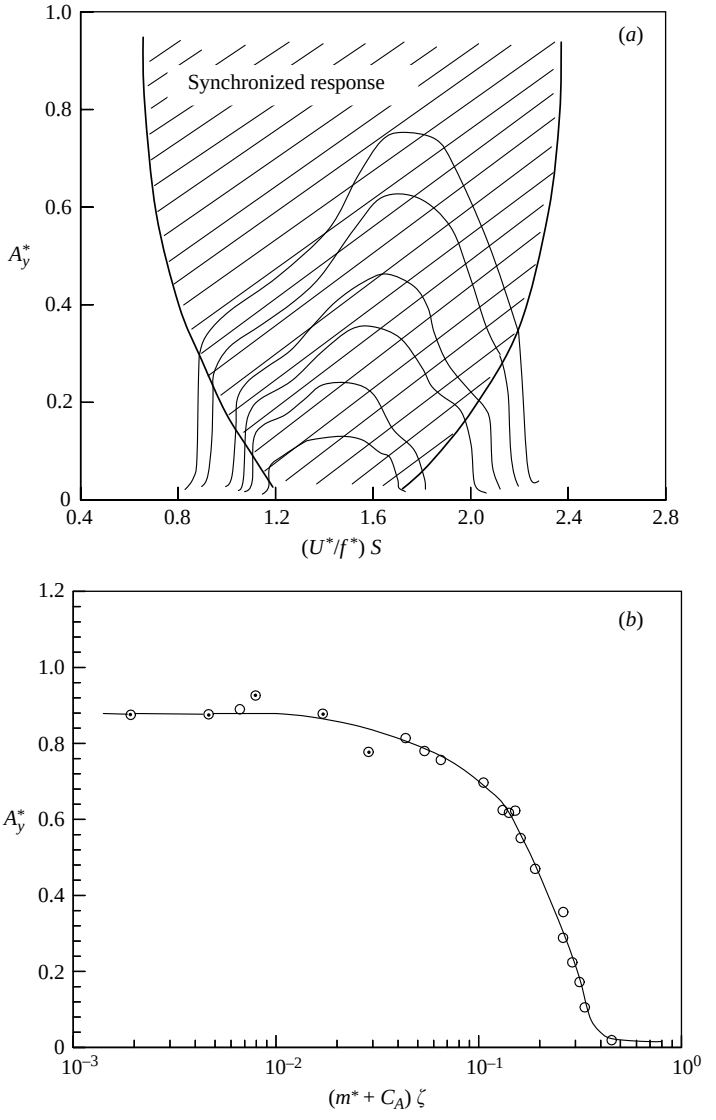

FIGURE 6. (*a*) Synchronized response regime and (*b*) the Griffin plot. The Griffin plot is a compilation of peak response amplitude data as a function of mass-damping parameter, $(m^* + C_A)\zeta$, and exhibits a saturation amplitude of $A_y^* \approx 0.9$, when $(m^* + C_A)\zeta < 0.02$. In this plot, the open symbols are for *y*-only motion; bull's eyes are for tethered (*xy*) spheres. The following parameters apply to (*a*) for increasing amplitude plots: $(m^* + C_A)\zeta = 0.333, 0.290, 0.261, 0.190, 0.151, 0.029$; $m^* = 198.4, 156.6, 60.6, 53.6, 27.5, 2.8$. *Re* at $A^*_{max} = 3800, 4500, 6300, 5300, 5500, 9100$. In (*b*), for decreasing $(m^* + C_A)\zeta$ below 0.02: *Re* at $A^*_{max} = 9100, 6800, 4000, 10500, 7700$.

magnitude from about 0.1, for a buoyant sphere in water, to about 1000, for a steel sphere in air.

3.1. *Effect of mass–damping parameter*

By systematically varying the mass–damping parameter, $(m^* + C_A)\zeta$, over a large range of values, a family of response plots was obtained, a few of which are shown in figure 6(*a*). As one might expect, from the form of equation (1.4), as one decreases

mass–damping, the peak response amplitude increases, and the regime of synchronization increases. This yields a (hatched) regime where synchronization may be found. The regime boundaries in figures 6(*a*) and 8 indicate the regime of significant periodic response. This regime is similar to the well-known synchronization region or 'lock-in' plots for the circular cylinder obtained from forced vibration studies by Koopmann (1967), Bearman & Currie (1979), and others, and shows the same general trend of a larger range of 'lock-in' (extent of $(U^*/f^*)S$), as the oscillation amplitude is increased. However, it is significant that the present synchronization region has been obtained from free vibrations, and hence, has the added criterion that there should be positive energy transfer to the body.

We compile a 'Griffin plot' in figure 6(*b*), showing the variation of the peak response amplitude (A_y^*) as a function of mass–damping parameter $(m^* + C_A)\zeta$. The plot suggests that a saturation amplitude of $A^* \approx 0.9$ is reached for low mass–damping, $(m^* + C_A)\zeta < 0.02$. Such a saturation amplitude has been discussed extensively by Griffin *et al.* (1982) and others for the circular cylinder. An important point to note from figure 6(*b*) is that, although the data points correspond to a large range of mass ratios ($m^* = 0.5 - 200$), they all seem to lie along a single curve when plotted using $(m^* + C_A)\zeta$, demonstrating that a combined mass–damping parameter is effective in collapsing the peak-amplitude data over a large range of values for sphere VIV.

It is also of relevance to note the relative insensitivity of the peak transverse amplitude (A_y^*) in this Griffin plot, even as the streamwise motion (A_x^*) increases up to 30% of A_y^*, for very low mass ratios (see figure 9). This is quite different from the cylinder VIV problem with two degrees of freedom in Jauvtis & Williamson (2004), where the presence of streamwise motion has a significant influence on transverse vibration. We also note that there is good agreement between the peak amplitudes for the tethered case (xy) and for the hydroelastic (y-only) case in the Griffin plot of figure 6(*b*), even down to very low mass ratios, $m^* < 1$.

As a final point concerning the Griffin plot, we observe that although the measurements are over a range of Reynolds numbers from $Re = 2000$ to 12 000, all the data seem to lie along a single line, indicating that there is no apparent Re effect on the response amplitude within this Re range. For example, at the saturation amplitude level, $(m^* + C_A)\zeta < 0.02$, the Reynolds numbers for the data points range from about 4000 to 10 500. Further evidence for this Reynolds number independence will be also seen in the next subsection.

3.2. *Effect of mass ratio*

An important effect of a reduction in mass ratio on the amplitude response of an elastic cylinder is the widening of the synchronization regime in U^*. We find very similar behaviour for the sphere, as shown in figure 7. Compared to the larger mass ratio ($m^* = 2.8$) case in figure 1, the synchronization regime for very low mass ($m^* = 0.45$) is significantly increased. In fact, the end of the synchronization could not be reached for the highest velocities possible in our water-channel facility. Further, as one might expect from the cylinder studies, the response frequencies (figure 7) become markedly higher as mass ratio is reduced showing in this case resonant vibration up to $f \sim 2f_N$.

When m^* is sufficiently small, we find the presence of a region of non-periodic response within the synchronization region for $U^* \approx 6$, as shown by the time trace in figure 7(*b*). On either side of this region, there are very periodic regimes in (*a*) and (*c*). The first of these periodic regions, centred around $U^* \approx 5$, is referred to as mode I, and corresponds to a flow velocity where the body vibration frequency (f) is in resonance with the natural frequency (f_N). One might expect the amplitude to keep

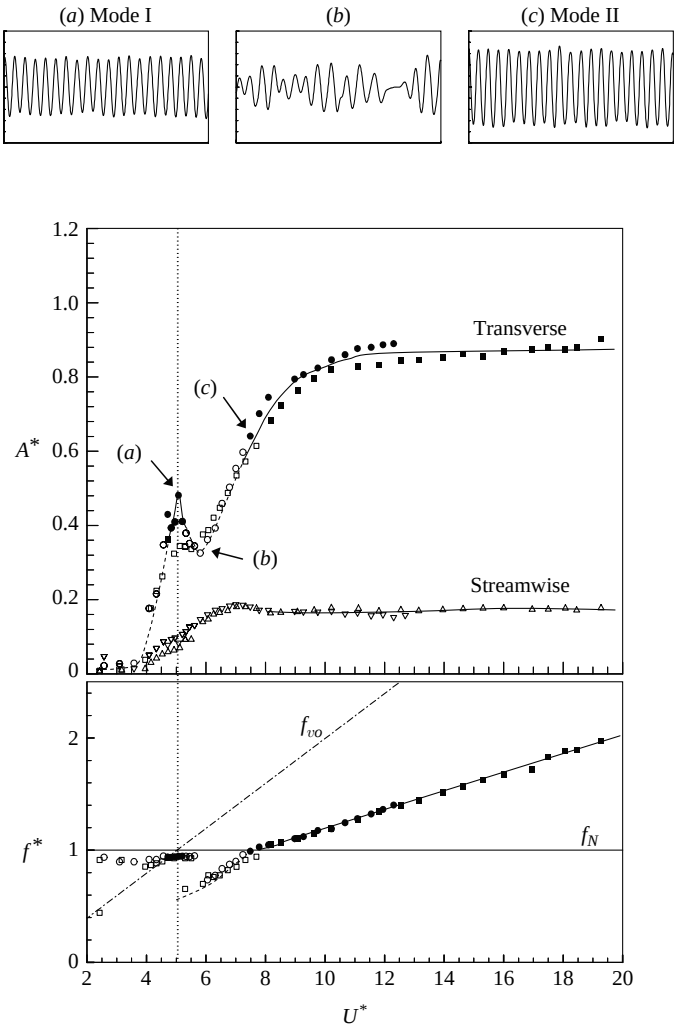

FIGURE 7. Typical amplitude and frequency response for a very light tethered sphere ($m^* = 0.45$). Solid symbols indicate highly periodic transverse vibration, while the transition regime (open symbols) shows the regime of non-periodic oscillations. ○, □, transverse response (tether length (L)/diameter = 5.9 and 13.8); ▽, △, streamwise response ($L/D = 5.9$ and 13.8). Re at $U^* = 5.0$ is 2000 for $L/D = 13.8$, and 3100 for $L/D = 5.9$.

decreasing as the flow speed is further increased. However, as reported in Williamson & Govardhan (1997), another mode of vibration, which we refer to as mode II, takes hold, and the amplitude again begins to increase, and reaches much larger values than before.

The response of a tethered sphere (xy-motion) at very low mass ratio, shown in figure 7, indicates that the principal motions are in the transverse direction ($A^*_{y\,max} \approx 0.9$), although we also find streamwise amplitudes ($A^*_{x\,max} \approx 0.2$). We compare, in figure 7, two different tether lengths (tether length/diameter = 13.8 and 5.9), which yield different natural frequencies (f_N), and hence different Re ranges. The collapse of the data suggests that the response is reasonably independent of Re within the Re range of interest ($Re = 2000$ to 12 000), as discussed earlier.

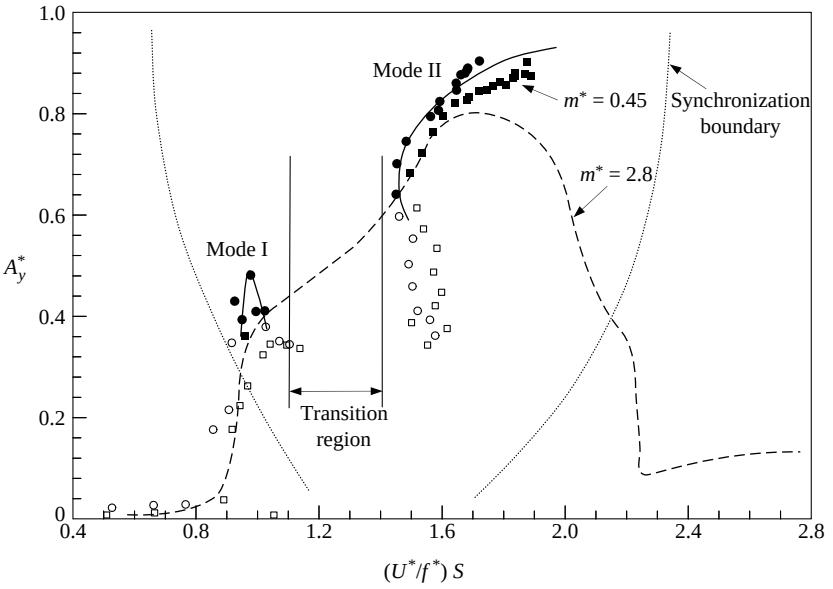

FIGURE 8. Amplitude response (of figure 7) plotted versus normalized velocity $(U^*/f^*)S$, exhibiting the distinct modes I and II separated by a jump. (Symbols as in figure 7). The dashed line shows the response for a higher mass, $m^* = 2.8$ without such a distinct transition.

When we plot amplitude against $(U^*/f^*)S$, instead of U^*, in figure 8, we find that the two periodic regions of response are markedly separated within the synchronization region. There are indeed two distinct modes of oscillation at this low mass ratio, $m^* = 0.45$, although at higher $m^* = 2.8$, the response seems to remain periodic and transition continuously from mode I to mode II, as represented by the dashed curve response.

Finally, the streamwise amplitude (A_x^*) is found to be dependent on the mass ratio, for sufficiently small mass, $m^* < 6$, as shown in figure 9. For larger sphere mass, $m^* > 6$, one may consider the streamwise amplitude as negligibly small.

4. Force measurements

Direct measurements of the fluctuating transverse force on the oscillating sphere were made for an elastically mounted sphere (y-only) for $m^* = 31$ and $(m^* + C_A)\zeta = 0.15$. In this section, we shall focus our attention on force measurements for the first two modes within the fundamental synchronization regime.

Before proceeding to look at the force measurements, we shall briefly introduce the 'vortex force', due only to the dynamics of vorticity, and the equations to compute it from the measured total force. As performed by Govardhan & Williamson (2000), based on the suggestions of Lighthill (1986) and several earlier studies, the total fluid force (F_{total}) can be split into a 'potential force' component $F_{potential}$, given in this case by the potential added mass force, and a 'vortex force' component (F_{vortex}) that is due to the dynamics of vorticity, where $F_{potential} = -[C_A m_d \ddot{y}(t)]$ and $m_d =$ displaced fluid mass. The vortex force F_{vortex}, can thus be computed from

$$F_{vortex} = F_{total} - F_{potential}. \tag{4.1}$$

Normalizing all the forces by $(\frac{1}{2}\rho U^2 \pi D^2/4)$ gives

$$C_{vortex}(t) = C_{total}(t) - C_{potential}(t), \tag{4.2}$$

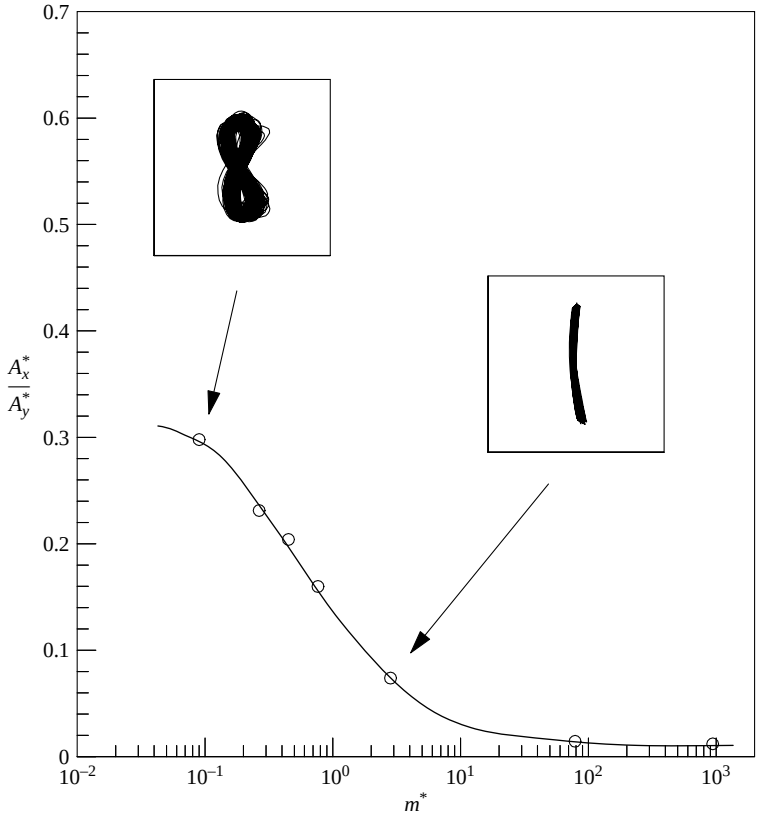

FIGURE 9. Normalized streamwise amplitude (A_x^*/A_y^*) as a function of the mass ratio (m^*), showing a smooth variation over four orders of magnitude in m^*. The ratio is measured for conditions of maximum A_y^*.

where $C_{potential}$ may be easily calculated from a knowledge of the instantaneous body acceleration $\ddot{y}(t)$. The vortex force coefficient, $C_{vortex}(t)$, may thus be calculated from the measured total force using equation (4.2). The concept of vortex force, or the relationship between impulse of vorticity and fluid momentum, has been extensively used in fluid mechanics (Lamb 1932; Moreau 1952; Batchelor 1967; and others), prior to Lighthill's work, and also discussed at length subsequently in Saffman (1992). The 'vortex phase' (ϕ_{vortex}) is, for the first time, introduced and defined in Govardhan & Williamson (2000) to be the phase between $C_{vortex}(t)$ and the body displacement, $y(t)$, while the conventionally used total phase (ϕ_{total}) is the phase between $C_{total}(t)$ and the body displacement, $y(t)$. One can now write two formulations for the equation of motion:

equation of motion using 'total force'

$$m\ddot{y} + c\dot{y} + ky = F_{total}\sin(\omega t + \phi_{total}), \tag{4.3}$$

equation of motion using 'vortex force'

$$(m + m_A)\ddot{y} + c\dot{y} + ky = F_{vortex}\sin(\omega t + \phi_{vortex}). \tag{4.4}$$

Obviously, these equations of motion assume a sinusoidal forcing which is only approximately correct. For non-sinusoidal fluid forcing, one would use the amplitude of the fundamental component of the fluid forces (at frequency ω).

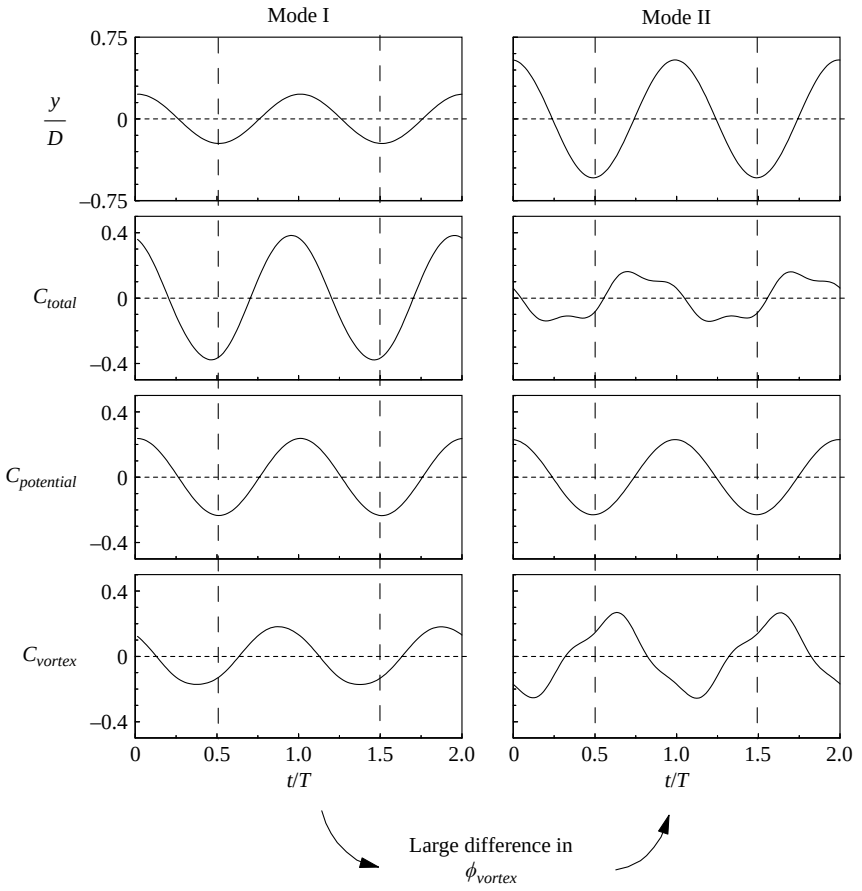

FIGURE 10. Relationship between total transverse force (C_{total}), the potential force ($C_{potential}$) and vortex force (C_{vortex}) for both mode I ($(U^*/f^*)S = 1.0$), and mode II ($(U^*/f^*)S = 1.7$). These measurements correspond with the bull's eye symbols ($\odot$) in figure 11.

We now select two values of normalized velocity, $(U^*/f^*)S = 1.0$ and 1.7, in figure 8, to represent conditions in the heart of mode I and mode II regimes (respectively). Although the transition between these two modes is continuous for these higher mass ratios, we expect these conditions to represent different phenomena for very low mass, where we found a distinct separation between modes I and II in figure 8. Cyclic variations of total, potential and vortex force are shown in figure 10 (phase-averaged). Immediately, one notes the large shift in the phase of the vortex force (ϕ_{vortex}) relative to body motion, $y(t)$. The shift in vortex phase is also evident in figure 11, indicating $\phi_{vortex} \sim 50^\circ$ when mode I is prevalent, and $\phi_{vortex} \approx 140^\circ$ when mode II has a peak amplitude at $(U^*/f^*)S = 1.7$. There is some similarity with the cylinder VIV case of Govardhan & Williamson (2000) in that ϕ_{total} passes through 90°, as the mode II response reaches a peak amplitude.

These results suggest that at very low mass ratios (e.g. our case for $m^* = 0.45$) there will be a *jump* in phase between the modes I and II, as indicated by figure 8 in the $\{(U^*/f^*)S,\ A_y^*\}$ plane. We shall now show in § 5 how the shift in vortex phase between the modes is the result of a clear shift in the timing of vortex formation. However, it is obvious that in both cases, despite the change in vortex timing, the vortex dynamics

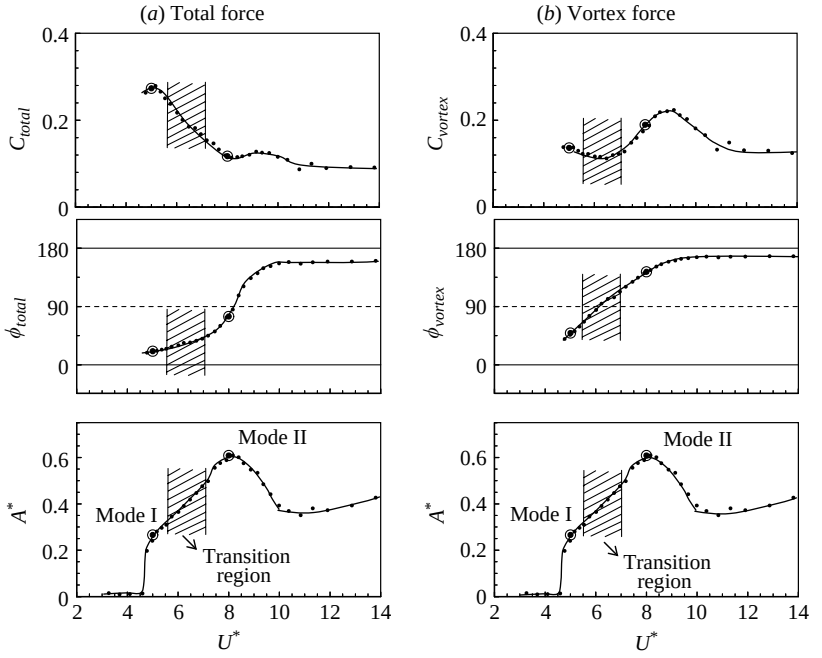

FIGURE 11. Force and phase angle variation with U^*: (*a*) total force, (*b*) vortex force. The $\odot$ symbols on the plots indicate locations in the heart of mode I and mode II regimes, outside the transition region between the two modes. ($m^* = 31.1$ and $(m^* + C_A)\zeta = 0.15$).

are such that there is a net positive energy transferred from the fluid to the body motion, to sustain vibrations.

5. Modes of vortex formation

Although there appear to be no previous visualizations of the wake of a transversely oscillating solid sphere, the recent work of Brücker (1999), on the wake of a rising bubble undergoing zig-zag motion, suggests that the wake consists of trailing vortices from which one may infer hairpin vortices. In the present section, we shall use DPIV measurements of the vorticity in the wake, in a manner similar to that of Brücker (1999, 2001), to show the hairpin vortex structure for both mode I and mode II sphere oscillations. Further, the streamwise vorticity measurements will be used to show a change in the timing of vortex shedding relative to body motion as we pass from mode I to mode II, which is consistent with the change in vortex phase seen in the previous section.

Extensive flow visualization has been carried out to observe the formation of vortex loops in the wake of the vibrating sphere, for the different modes. We include only one example here, in figure 12, which demonstrates the principal vortex loops observed simultaneously from two orthogonal directions. A common phenomenon with all the visualizations is the fact that the heads of the loops pinch off (at a point several diameters downstream) to form vortex rings, and we discuss this later. However, close to the body, we have measured the streamwise vorticity in a plane normal to the flow and at $1.5D$ downstream of the sphere centre, to yield the dominant counter-rotating streamwise pairs in figure 13, for both modes. As the sphere oscillates, the strength of the vortex pair reduces and a pair of opposite sign is generated on the other side of the

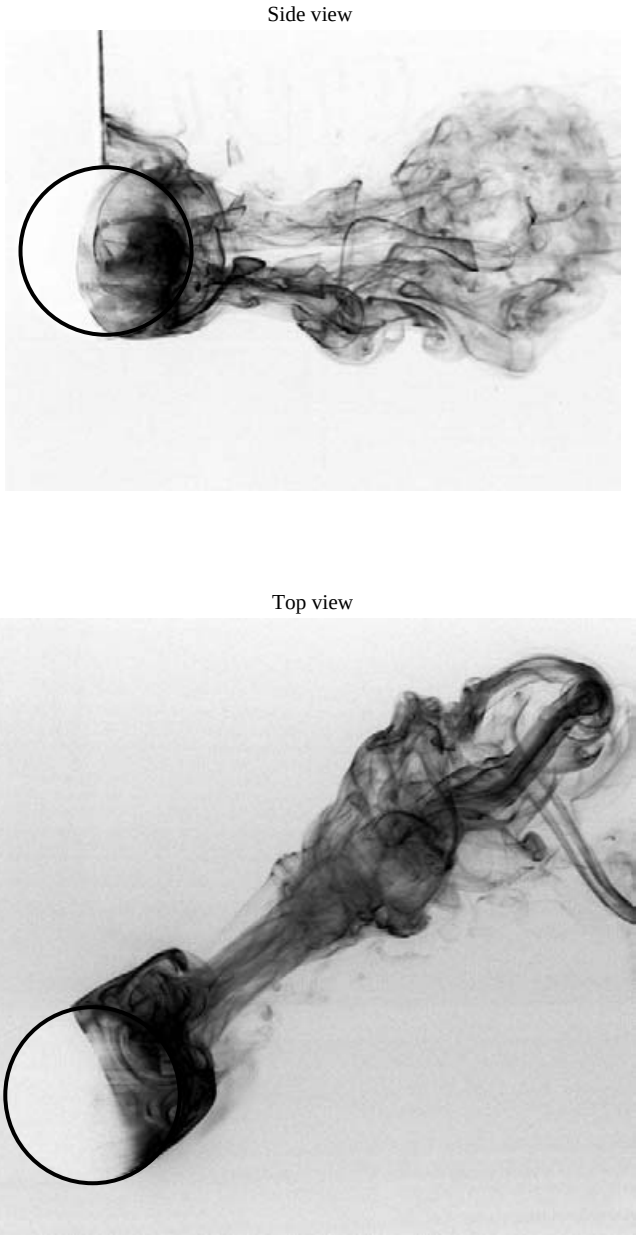

FIGURE 12. Flow visualization of the wake of a vibrating sphere, showing streamwise vortex loops and the development of a vortex ring at the end of the loop. The dynamics are for mode II, $A_y^* = 0.90$; $(U^*/f^*)S = 1.80$; $Re = 2000$.

body. This is consistent with the formation of a chain of vortex loops, on both sides of the wake. (It should be noted that, in figure 13, the location of the sphere has been adjusted, in an approximate manner, for the time taken by the vortex structure to convect to the plane where vorticity is measured, using a convection speed (U_v) computed from vorticity dynamics in the equatorial plane (see figure 15)). The distinct differences in the timing of vortex pair formation for modes I and II, in figure 13, is consistent with differences in the vortex phase between the modes, found earlier in figure 10.

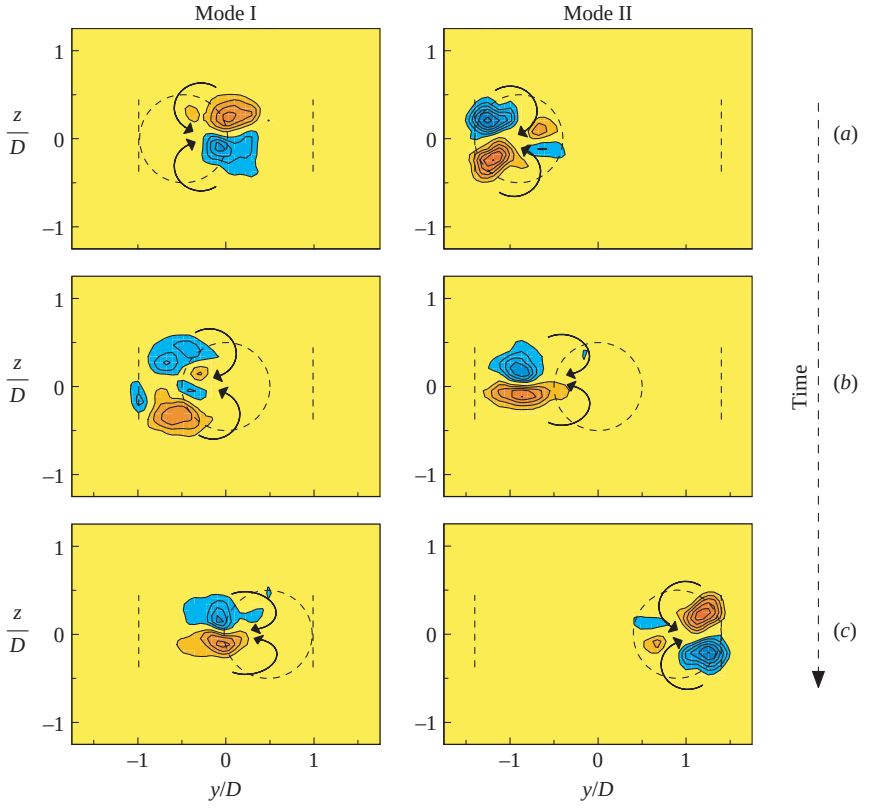

FIGURE 13. Streamwise vorticity plots showing the dominant counter-rotating vortex pair in both mode I and mode II. Each of these plots from cross-sectional DPIV measurements are separated by a quarter-period, and were measured at $x/D = 1.5$. Blue contours show clockwise vorticity, red anti-clockwise vorticity. Contour levels shown are $\omega D/U = \pm 0.3, \pm 0.6, \pm 0.9, \ldots$. Mode I: $(U^*/f^*)S = 0.98$, $A^* = 0.50$, mode II: $(U^*/f^*)S = 1.80$, $A^* = 0.90$. $Re \approx 3000$ in both cases.

A spatio-temporal reconstruction of the sphere wake has been made in figure 14, employing 16 streamwise vorticity fields for each half-cycle of sphere oscillation. (We also use for the image a convection velocity U, so that time t is converted into streamwise location, $x = Ut$). The resulting three-dimensional structure clearly exhibits a two-sided chain of vortex loops for each mode.

In both modes I and II, the vorticity structure of figure 14 indicates the development of a vortex ring at the head of the vortex loop, due to the pinching off and vortex reconnection of the two sides of the loop. By observing the vertical vorticity in the equatorial plane in figure 15 (i.e. looking vertically downwards in the water channel), we can see a horizontal 'cut' through the developing vortex ring, showing the formation of both signs of vorticity. Interestingly, the vertical vorticity in the equatorial plane resembles the 2P mode of vortex pair formation in the case of the vibrating cylinder (Williamson & Roshko 1988), although its formation is slightly further downstream than for the vibrating cylinder.

A schematic diagram of the pinching off and vortex reconnection at the head of a vortex loop is shown in figure 16. Such a vortex reconnection resembles the manner by which vortex rings are formed out of a pair of vortices, when subjected to the long-wavelength Crow instability (see, for example, Leweke & Williamson 2004).

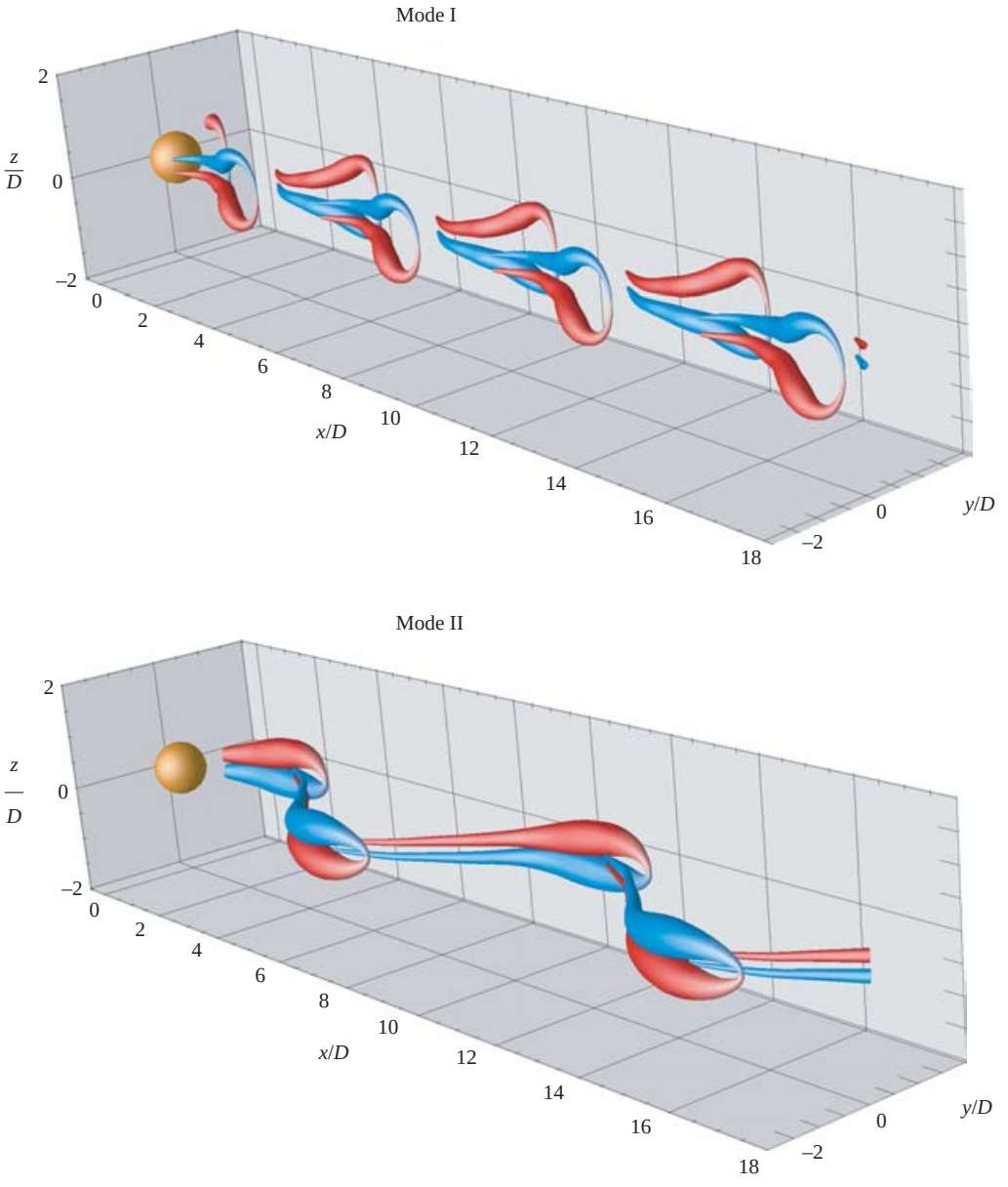

FIGURE 14. Three-dimensional reconstruction of the sphere wake from the measured time sequence of streamwise vorticity. For both modes, the three-dimensional structure clearly shows that the wake comprises a two-sided chain of streamwise vortex loops. Blue indicates clockwise vorticity, and red anti-clockwise vorticity. $Re \approx 3000$.

The formation of interlinked vortex rings is a phenomenon seen in the fascinating dye visualizations of Magarvey & Bishop (1961) in the wake of a liquid drop, and also observed in computations of a sphere wake by Mittal (1999) at lower Reynolds numbers of around 500. Interlinked vortex loops are a feature of the computations of Tomboulides, Orszag & Karniadakis (1993), and also of the experiments of Sakamoto & Haniu (1990), Ormières & Provansal (1999) and in the very clear

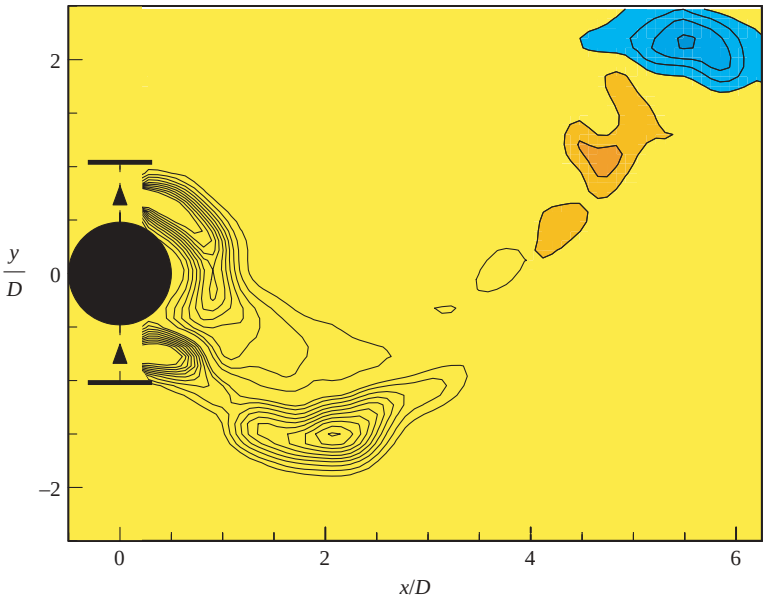

FIGURE 15. Equatorial-plane vorticity plot showing the presence of a counter-rotating vortex pair downstream that represents a cut through a vortex ring. Coloured blue contours show clockwise vorticity, red anti-clockwise vorticity. Contour levels shown are $\omega D/U = \pm 0.25$, ± 0.5, ± 0.75, ... $Re \approx 3000$, $(U^*/f^*)S = 1.80$.

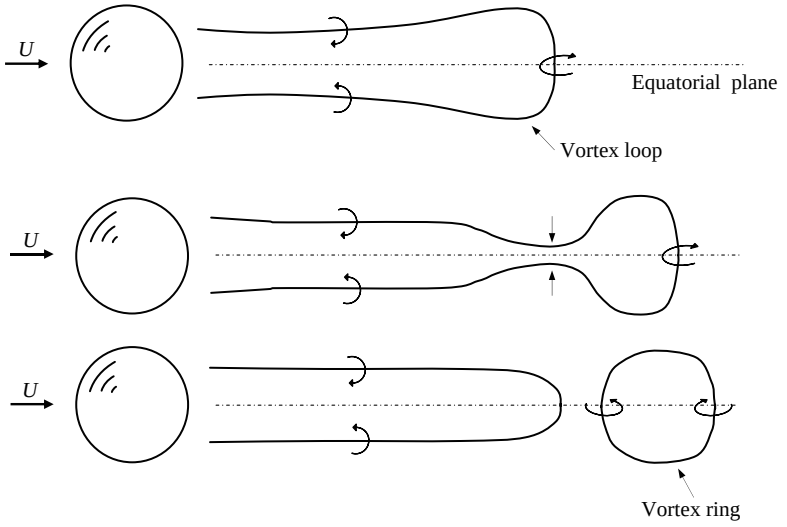

FIGURE 16. Diagram showing pinch-off and vortex reconnection leading to formation of a vortex ring at the downstream end of a vortex loop.

visualizations of Leweke *et al.* (1999), all concerned with the wake of a static sphere. A two-sided chain of (alternating sign) vortex loops has been observed experimentally in the range $Re > 800$ by Sakamoto & Haniu (1990), quite analogous to our results here. However, there is a central distinction between the wake behind a static sphere and the flow here; namely that in the natural (static) case, the vortex loops are

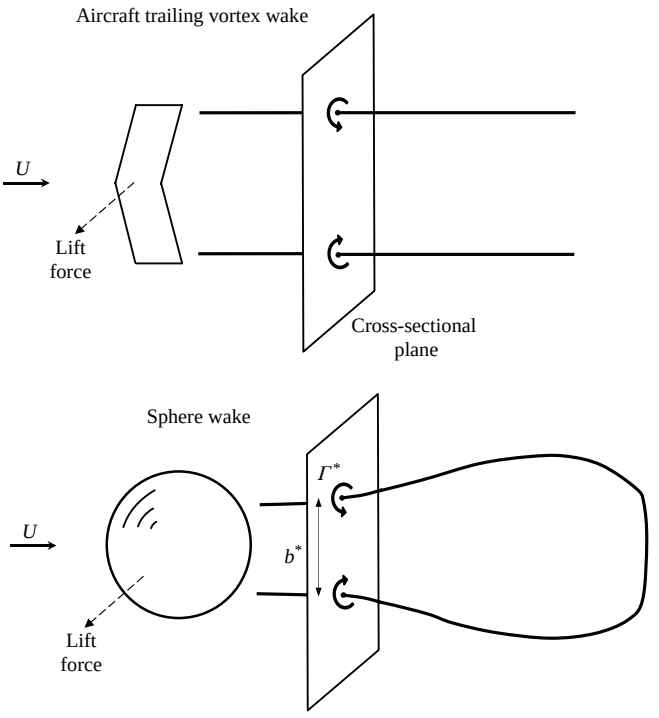

FIGURE 17. Diagram which highlights the analogy between the aircraft trailing vortices and the sphere streamwise vortex pair, both of which yield a lift force on the body. The upper vortex of strength Γ^* is situated a distance b^* from its counter-rotating vortex.

formed in a somewhat irregular fashion, and the azimuthal location, at which loops are formed changes slowly from cycle to cycle, as summarized by Mittal (1999).

In the case of the present vortex-induced vibrations of a sphere, there is obviously a preferred orientation of the loops to maintain a symmetry with the (horizontal) plane containing the principal transverse vibrations. We observe that as the sphere accelerates to one side (transverse to the flow), the vortex pair orients itself such that one vortex is vertically above the other, so that approximately the horizontal plane acts as a plane of symmetry. This particular arrangement of vortex pairs (as opposed to being oriented at some other azimuthal angle), would give rise to a transverse (lift) force, consistent with the sphere transverse vibrations, rather like the vertical lift force associated with aircraft trailing 'tip vortices'.

6. Analogy with wing trailing vortices: prediction of lift force

The principal vortex structure coming out of the vortex formation region behind the vibrating sphere appears to be counter-rotating vortex pairs (with secondary structures as an auxiliary feature). These streamwise vortex pairs are aligned approximately with the free stream, in a manner similar to trailing vortices behind aircraft wings. As a result of this observation, we approach a prediction of transverse force, or 'lift' force on the body, in the same manner as one might compute the lift on an aircraft wing from a knowledge of the strength and spacing of the trailing 'tip' vortices. We represent this vortex pair structure behind the sphere and a wing in figure 17, indicating the sense of the lift force that is expected. It can be deduced that the lift

force (see, for example, Saffman 1992) can be given by the following expression:

$$F_{vortex} = -\rho U_v \Gamma b, \tag{6.1}$$

where F_{vortex} is the vortex force; U_v is the convection speed of the trailing vortices (typically $U_v/U = 0.5$ at the location where we measure streamwise vorticity); Γ is the strength of the upper vortex in figure 17; and b is the spacing between the vortices. This expression may be derived from considerations of the rate of change of transverse impulse due to the streamwise vorticity distribution. Here we use the expression in a quasi-steady manner, using the approximation that the instantaneous force $F(t)$ depends only on the instantaneous values of $[\Gamma(t), U_v(t), b(t)]$. We may normalize the force by $(\frac{1}{2}\rho U^2 \pi D^2/4)$ to give

$$C_{vortex} = \frac{8}{\pi} U_v^* \, b^*(-\Gamma^*), \tag{6.2}$$

where $U_v^* = U_v/U$; $b^* = b/D$; $\Gamma^* = \Gamma/(UD)$. The speed (U_v^*) and spacing (b^*) remain positive at all times, so that $C_{vortex} \leqslant 0$ when $\Gamma^* \geqslant 0$. We may understand the vortex force in a physical manner, by considering the 'downwash' fluid motion between the vortices. For a positive upper vortex, the 'downwash' between the vortices flows to the right, and thus the force is to the left when looking upstream.

Evaluation of this vortex force is made in figure 18 for each of the modes I and II from vorticity measurements behind an elastically mounted (y-only) sphere, and has a reasonable agreement with the directly measured force using the force balance. Both the magnitude and phase of the vortex force compare quite well. The principal conclusion one might draw from this agreement is the fact that most of the transverse force on a sphere is given by the dynamics of the streamwise vorticity. The orientation of the trailing vortex pair in the near wake appears to yield the direction of the force on the body. Therefore, we might also conclude that the vortex-induced vibrations of such a three-dimensional body are induced by the streamwise vorticity, which is quite distinct from bodies such as the cylinder whose dynamics are induced by vorticity normal to the flow.

We note that the spacing between the vortices reaches a maximum when the strength of each vortex pair is a maximum. However, the phase of maximum vortex force is quite distinct for each mode, as noted in figure 18; the force is roughly in phase with body oscillations for mode I and almost out of phase for mode II. This is consistent with earlier measurements of vortex phase (ϕ_{vortex}) in figure 11.

7. Periodic oscillations at high $(U^*/f^*)S$: mode III response

A remarkably periodic and robust mode was unexpectedly discovered in the regime $(U^*/f^*)S = (f_{vo}/f) = 3$ to 8, by Jauvtis *et al.* (2001), whose response amplitude plot is shown in figure 19(*a*). There is no equivalent mode for the cylinder VIV, and we note that it represents a low-oscillation frequency (f) relative to the frequency of vortex formation (f_{vo}) for the static sphere. In other words, we have a highly periodic vibration of the sphere over a wavelength for which the static body would exhibit between 3 and 8 vortex structures. We can see multiple small-scale structures in the flow visualization, typical of mode III, in figure 19(*b*). No clear structure could be simply associated with a half or full wavelength of the sphere vibration from these extensive studies. However, streamwise vortex structures appeared to remain as a thread underlying the multiple smaller vortices.

Somehow the flow must yield a forcing on the body at this low frequency, sufficient to deliver a net energy transfer into the body motion. If one assumes that the

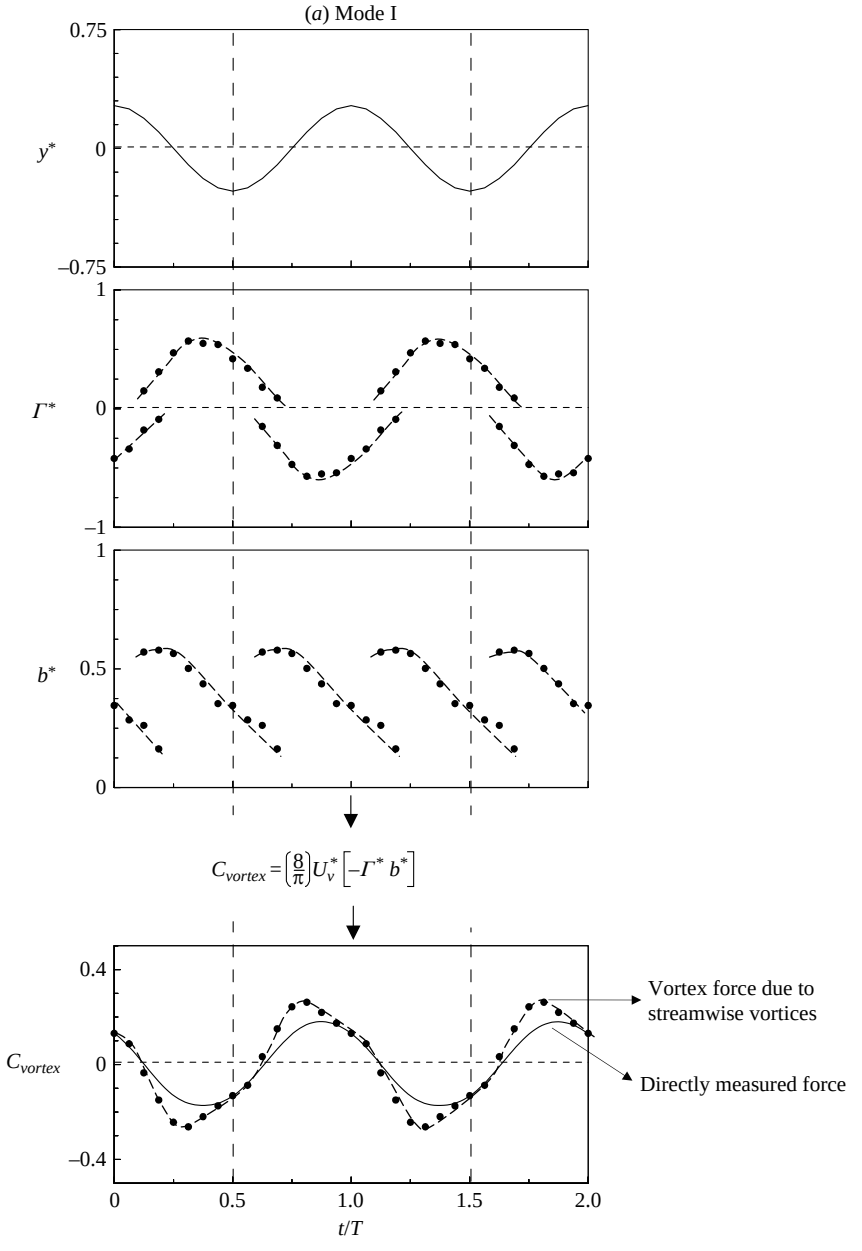

FIGURE 18(*a*). For caption see facing page.

transverse displacement and vortex force are represented by the following functions:

$$y(t) = A\sin(\omega t), \tag{7.1}$$

$$F_{vortex}(t) = F_o \sin(\omega_o t + \phi), \tag{7.2}$$

then one can show, as in Jauvtis & Williamson (2004), that the net energy transfer over a cycle of body oscillation (E) is given by

$$E = (F_o A\omega)\sin\phi \int_0^T \cos(\omega t)\cos(\omega_o t)\,\mathrm{d}t. \tag{7.3}$$

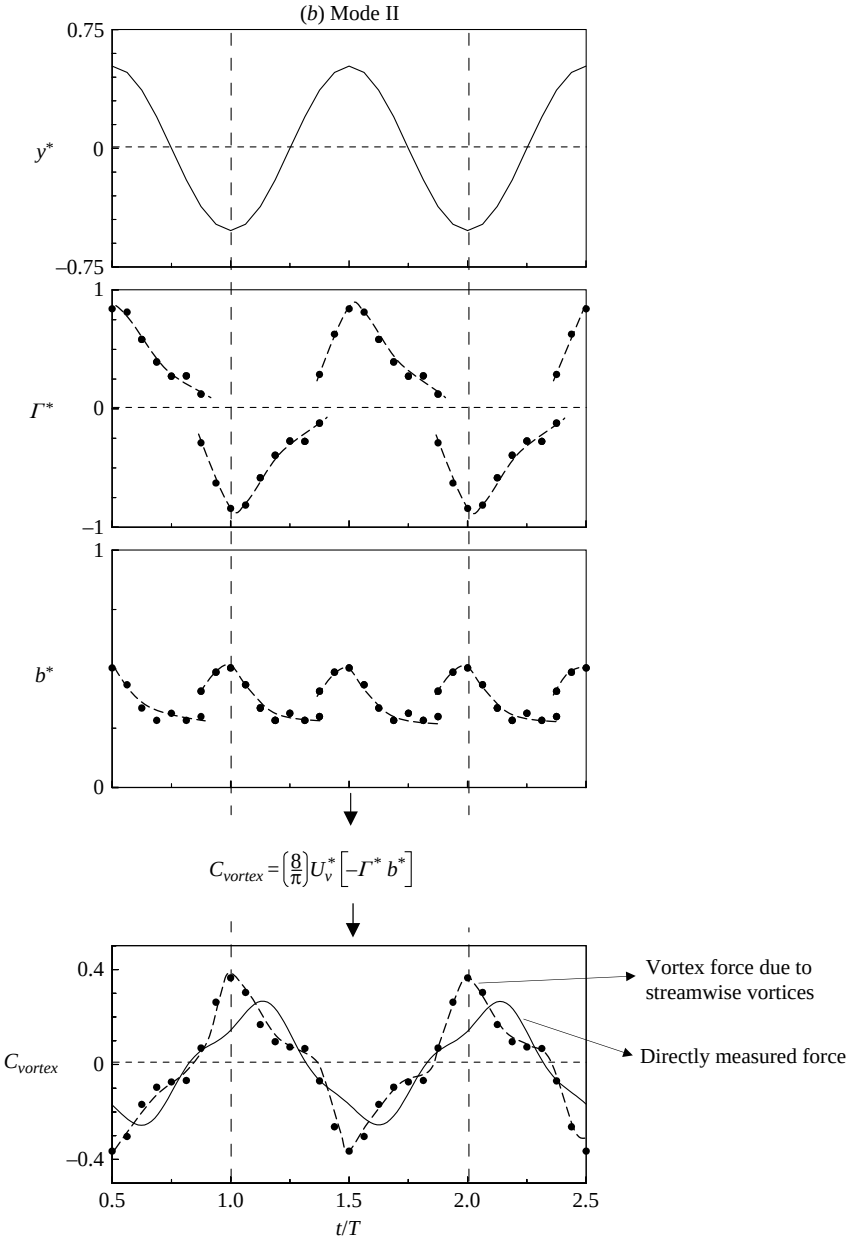

FIGURE 18. Vortex force (C_{vortex}) is evaluated using the analogy with airplane trailing vortices. Predicted vortex force compares reasonably well with direct force measurements (solid line in lowest plot), using equation (6.2). (*a*) Mode I: in this case, $(U^*/f^*)S = 1.0$, corresponding to mode I in figure 10. (*b*) Mode II: in this case, $(U^*/f^*)S = 1.7$, corresponding to mode II in figure 10. $Re = 3000$ in both (*a*) and (*b*).

This integral is only non-zero if $\omega = \omega_o$. In other words, as one might expect, the body vibrates because there is a component of the vortex force that is synchronized with the body oscillations. We seek to identify the repeatable vortex dynamics underlying the phenomena, and to further characterize the mode with direct force measurements.

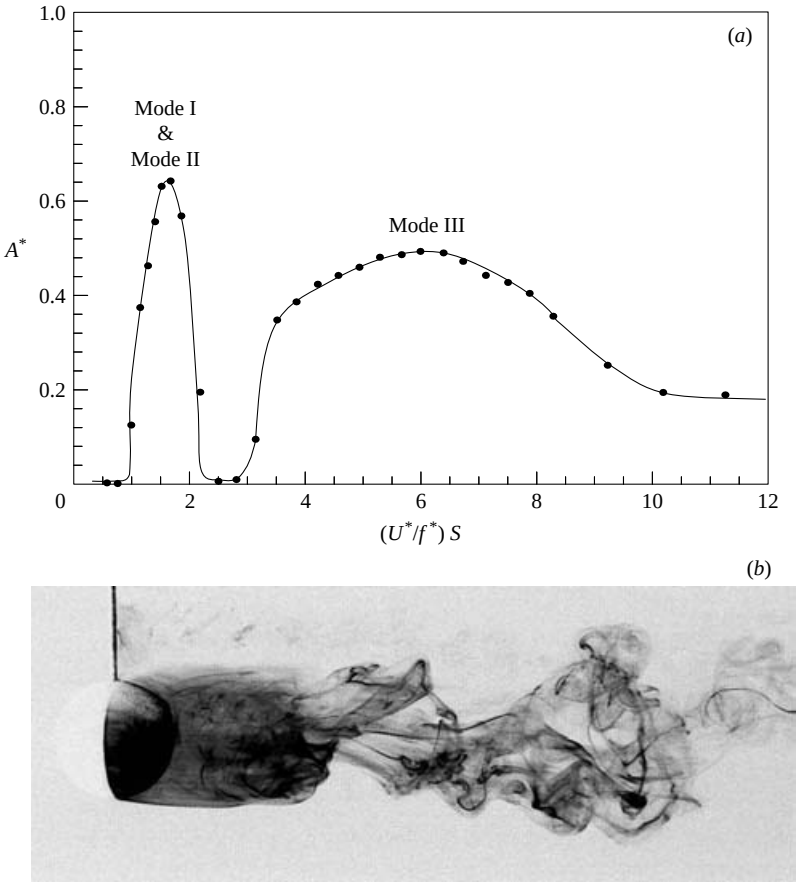

FIGURE 19. Amplitude response and flow visualization for mode III vibrations. The amplitude response in (*a*) shows the huge extent of the periodic mode III oscillations, made evident by noting how narrow the modes I and II appear in this plot. $m^* = 75$, $(m^* + C_A)\zeta = 0.14$. The flow visualization in (*b*), shows multiple vortex structures per half-cycle of oscillation, that are not synchronized with the body motion. $(U^*/f^*)S = 3.5$; $A^* = 0.40$. Re at A^*_{max} in mode III = 9000.

As with mode I and II, we measure streamwise vorticity in the same manner, and find for mode III in figure 20 a clear wake structure locked with the body frequency, namely a two-sided chain of trailing vortex pairs as for the other modes. This is demonstrated by the spatio-temporal reconstruction of the vorticity into the remarkably long vortex loop structures in figure 20.

These vortex dynamics give rise to a net energy transfer from the fluid force into the body motion, as shown in figure 21, where we again evaluate the vortex strength Γ^* and vortex force C_{vortex} as a function of time. The normalized rate of energy transfer (or 'power in') is given by

$$\dot{e}_v = C_{vortex}\,\dot{y}^*, \tag{7.4}$$

where $y^* = y/D$, so we can combine this with equation (6.2) to give

$$\dot{e}_v = \frac{8}{\pi} U_v^* b^* [-\Gamma^* \dot{y}^*]. \tag{7.5}$$

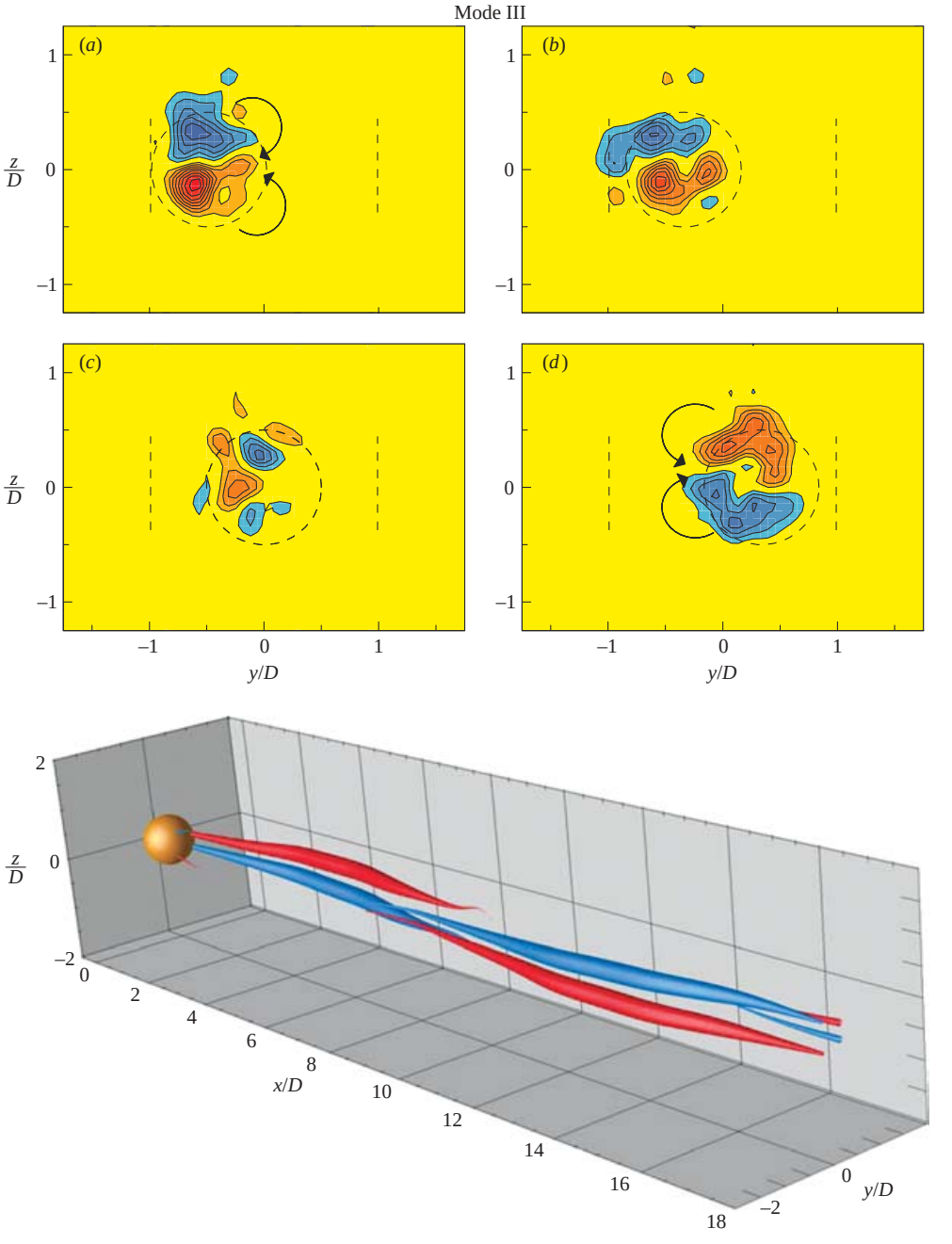

FIGURE 20. Phase-averaged streamwise vorticity plots for mode III at $x/D = 1.5$, showing that there exist repeatable streamwise vortex structures in the near wake. Each of the sequential vorticity plots (a) to (d) is separated by a quarter period. The streamwise vorticity is measured at the downstream location $x/D = 1.5$. Also shown is a three-dimensional reconstruction of the streamwise vortex structure that is synchronized to the low oscillation frequency. Blue shows clockwise vorticity, red counter-clockwise vorticity. Contour levels shown are $\omega D/U = \pm 0.3$, ± 0.6, ± 0.9, ... $(U^*/f^*)S = 3.5$, $A^* = 0.40$. $Re \approx 3000$.

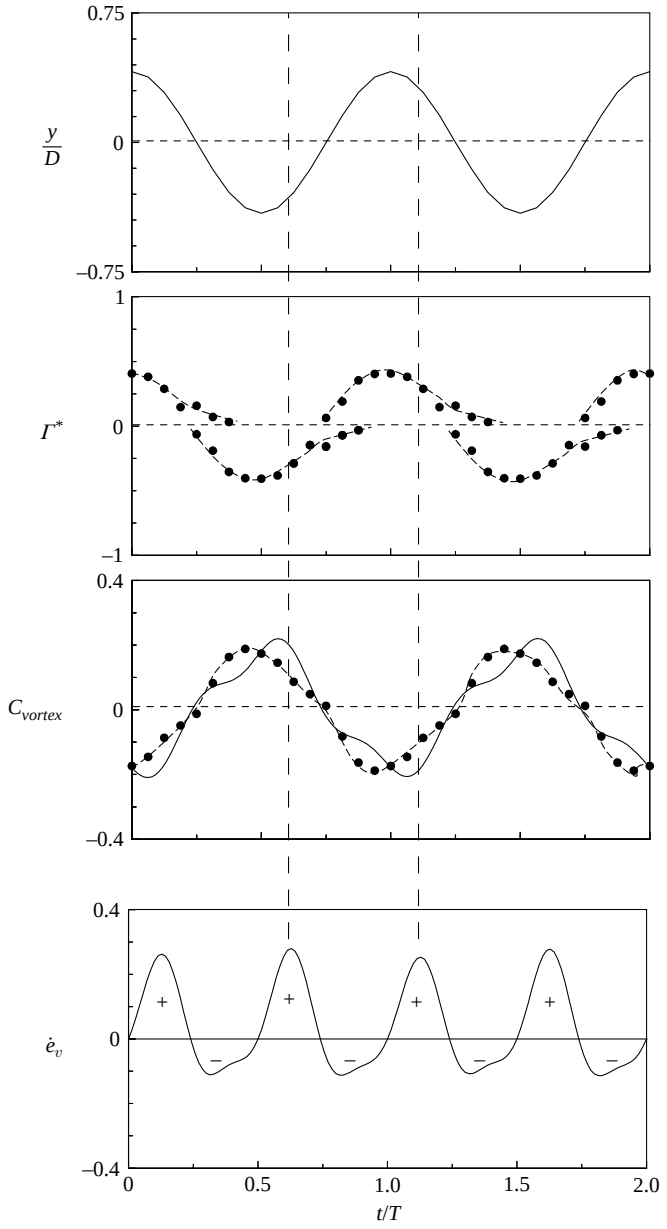

FIGURE 21. Vortex force and energy transfer in mode III. Phase-averaged force (C_{vortex}) showing clearly that there exists a component of the force at the low body oscillation frequency. The energy transfer ($\dot{e}_v$) indicates that there is net positive energy transfer to the body over an oscillation cycle. Solid C_{vortex} curve is from direct force measurement.

With the body at its maximum negative extreme position, $y^* = -0.5$ in figure 20(a) we then have zero velocity, $\dot{y}^* = 0$, and thus the energy transfer is zero, $\dot{e}_v = 0$. If we now consider case (c) in figure 20, $\dot{e}_v \sim 0$ because the net vortex pair strength is small, $\Gamma_{net} \sim 0$. On the other hand, between (a) and (c), we have a maximum energy input into the body motion when $\dot{y} > 0$ and $\Gamma^* < 0$, corresponding to case (b) in figure 20. The main point to be made is that there is an underlying streamwise vortex structure

which is synchronized with the sphere vibration frequency, and which yields a net positive energy transfer into the vibration over a cycle, allowing a highly periodic mode III vibration to ensue.

In essence, it seems that the tethered, or elastically mounted, sphere is intrinsically unstable. In the absence of vibration in mode III, there would be no specific forcing at the low natural frequency of the structure. However, if the body is perturbed, and vibrates in the transverse direction, it generates a self-sustaining vortex force to amplify and saturate the body vibrations, to possibly large amplitudes. In this manner, it represents an example of 'movement-induced excitation' categorized by Naudascher & Rockwell (1994). It should also be mentioned that broad low frequencies were measured in the streamwise vortex formation by Brücker (2001) for a static sphere, and so the sphere wake is naturally responsive to low-frequency disturbances.

8. Existence of a critical mass for sphere VIV

It has recently been discovered that a critical mass exists, for the case of vortex-induced vibrations of a cylinder, below which a large-amplitude response will persist up to infinite normalized velocity (see review of Williamson & Govardhan 2004). This surprising result shows that there is an infinitely wide regime of U^* for resonance. It was deduced that all vortex-induced vibration systems, that are represented well by equations (1.1)–(1.3), will necessarily exhibit a critical mass (m^*_{crit}). The numerical value of the critical mass is determined by the maximum negative value of the effective added mass (i.e. by the minimum of C_{EA}) within the regime of significant vibration in the amplitude response plot. For a transversely vibrating cylinder, the critical mass takes on the value $m^*_{crit} = 0.54$. It must be noted carefully that this result (in Govardhan & Williamson 2000, 2002) is valid for low mass–damping, $(m^*\zeta) < 0.05$. We might perhaps expect a critical mass of this order of magnitude for the tethered or elastically mounted sphere.

In the present case of the sphere, we compute C_{EA}, from frequency responses, at low $m*$, of the type shown in figure 1, using equation (1.5) such that

$$C_{EA} = m^* \left(\frac{1 - f^{*2}}{f^{*2}} \right) + \left(\frac{C_A}{f^{*2}} \right). \tag{8.1}$$

The critical mass ratio (m^*_{crit}) may be determined, as given by Govardhan & Williamson (2002), by evaluating the maximum value of $-C_{EA}$ that can be provided by the vortex dynamics, where the maximum is taken over all the points on the synchronized part of the amplitude response. The reason for this may be explained using the frequency equation (1.5) which is recalled below:

$$f^* = \sqrt{\frac{(m^* + C_A)}{(m^* + C_{EA})}}.$$

As m^* is gradually reduced, the term $(m^* + C_{EA})$ will first become zero at a point on the amplitude response with the largest $-C_{EA}$, and the frequency response f^* will then tend to infinity.

The evaluated C_{EA} from two low-mass-ratio responses shown in figure 22 indicates that the most negative value of C_{EA} is between -0.55 to -0.65 at low mass–damping ($(m^* + C_A)\zeta < 0.04$). Also, shown in the figure is C_{EA} data from the recent detailed experiments of Horowitz & Williamson (2005) for unrestrained rising spheres, where

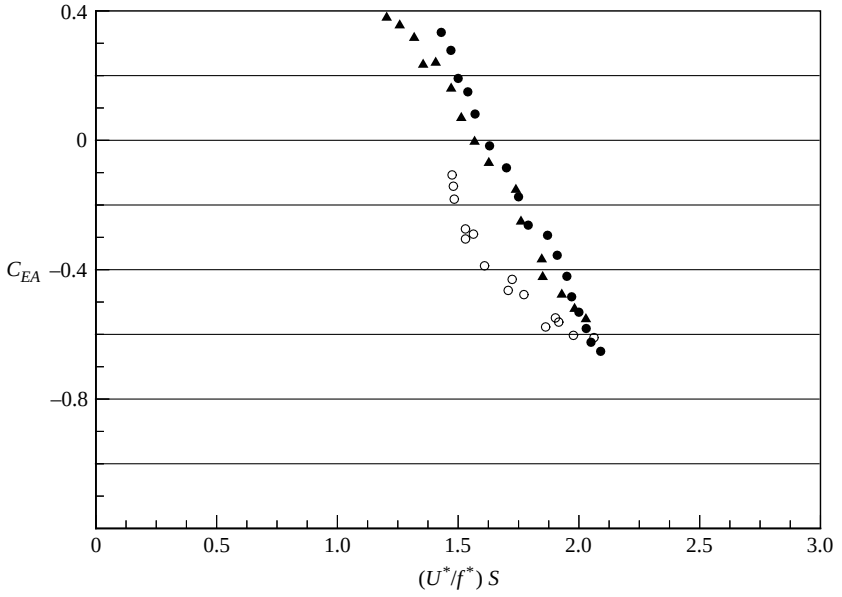

FIGURE 22. Evaluation of effective added mass (C_{EA}) and critical mass (m^*_{crit}). Calculated values of C_{EA} from frequency responses of low-mass-ratio elastically mounted spheres, and unrestrained rising spheres. In both cases, the minimum value of $C_{EA} \approx -0.6$, thus yielding a critical mass, $m^*_{crit} = [-C_{EA}]_{max} \approx 0.6$. ●, ▲, elastically mounted sphere ($m^* = 1.31$ and $m^* = 2.83$); ○, unrestrained rising sphere (Horowitz & Williamson 2004).

$U^* = \infty$. In this unrestrained (no restoring force) case, C_{EA} values have been evaluated using the relation: $C_{EA} = -m^*$, as discussed in Govardhan & Williamson (2002). The data for the unrestrained sphere yields a critical mass of $m^*_{crit} = 0.61$. Given the intrinsic imprecision in measuring C_{EA} from frequency responses in the present study, we may deduce an approximate value of critical mass as

$$m^*_{crit} = 0.6 \pm 0.05.$$

When we have a light sphere, whose mass is below critical, the frequency (f^*) increases continuously as flow velocity (U^*) is increased, such that the parameter $(U^*/f^*)S$ approaches an asymptote. This point is defined as the 'Operating point' by Govardhan & Williamson (2002), and is further discussed in that paper. The main point here is that we predict the large-amplitude response will persist to infinite U^*, if $m^* \leqslant 0.6$ for the elastically mounted sphere. In the case of the tethered sphere, these deductions are valid for large U^*, but not necessarily if that also induces large tether angles (the angle by which the tether leans over due to sphere drag). In that case some influence on the numerical value of the critical mass is expected.

Critical mass appears to be generic to VIV systems, as discussed in Govardhan & Williamson (2002) and in the review of Williamson & Govardhan (2004). For example it takes on the value 0.54 for a cylinder in transverse vibration, 0.52 for a cylinder in two degrees of freedom, 0.5 for a pivoted cylinder, and approximately 0.6 for the sphere VIV. It is noted that the values are (at least) valid for moderate Reynolds numbers (typically $Re \sim 2000$ to 20 000), and for low mass–damping ($m^*\zeta < 0.04$) for these VIV systems.

9. Concluding discussion

Despite the extensive research concerning cylindrical bodies in vortex-induced vibration, there have been very few studies regarding vibrations of tethered structures, even though tethered bodies are a common configuration. In this paper, we have studied the case of an elastically mounted sphere, induced to vibrate by its own vortical wake, in a motion transverse to a free stream. In parallel, we have investigated the vortex-induced vibrations of a tethered sphere, which principally involves vibration both streamwise and transverse to the flow. In these problems, we have been able to measure displacement, as well as force and vorticity dynamics, all simultaneously.

When the oscillation frequency (f) is of the order of the static-body vortex shedding frequency (f_{vo}), there exist two modes of periodic large-amplitude oscillation, defined as modes I and II, separated by a transition regime exhibiting non-periodic vibration. In the case of the very light tethered body, the transition between modes is quite distinct, especially when the response amplitude is plotted versus the parameter $(U^*/f^*)S$, where a jump between modes is clearly exhibited. In the case of elastically mounted bodies of higher mass, the transition between modes is more continuous, and the transition is only evident as a dip in the amplitude response plot. From our direct measurements of force (which necessarily has been done for the somewhat higher mass ratios), we have observed that the phase of the vortex force relative to sphere dynamics is quite different between the modes I and II. This difference in the phase of the vortex force is consistent with the large difference in the timing of the vortex formation between modes, which was observed from the vorticity measurements for the light sphere vibrations.

The dominant wake structure for both modes is a chain of streamwise vortex loops on alternating sides of the wake. Streamwise vorticity was measured in the near-wake formation region of the sphere, and we performed a spatio-temporal reconstruction of the streamwise vorticity structures to show vividly, in three dimensions, the principal chain of streamwise vortex pairs, which are synchronized at the sphere vibration frequency. The induced vibration of the body locks in a particular preferred orientation for the vortex loops, to maintain symmetry with the (horizontal) plane containing the principal body displacement. This is unlike the azimuthal wandering of the wake structures behind static spheres, which have been observed from flow visualization or from numerical simulations at low Reynolds numbers, as discussed by Mittal (1999).

Flow visualization further downstream shows that the heads of the vortex loops pinch off to form a sequence of vortex rings. Vorticity in the equatorial plane (the plane of symmetry between each streamwise vortex in a given pair) shows the development of the pinching-off process, which yields counter-rotating vortex pairs in this plane. The appearance of this vorticity distribution is not unlike the 2P mode of vortex dynamics for the cylinder VIV, where one has two pairs of vortices each cycle of body vibration (Williamson & Roshko 1988). However, in the present case, the two vortex pairs in the equatorial plane represent a cut through a pair of vortex rings, and we might define the vortex mode evolving further downstream as a '2R' mode, or two vortex rings per cycle of body motion, in analogy with the cylinder vortex mode.

If one looks upstream from directly behind the vibrating sphere, at a plane normal to the flow, where particle motions are illuminated, it is immediately apparent that in all modes, there is a synchronized streamwise vortex pair formation in each half-cycle (as measured above). However, what immediately struck us in observing this flow in real time, is that the dynamics appear just like those vortex motions behind a wing,

namely a trailing vortex pair. In the case of the wing, one can predict the lift force by considering the rate of change of impulse for the streamwise vortex pair. We therefore employ a quasi-steady assumption, and compute the normalized 'lift' (or transverse vortex force) on the sphere,

$$C_{vortex} = \frac{8}{\pi} U_v^* b^* (-\Gamma^*),$$

where vortex strength Γ^* and vortex spacing b^* are measured as a function of time. We find a reasonable agreement between these predictions and direct force measurements, which is significant because it indicates that the principal vorticity dynamics giving rise to vortex-induced vibration for a sphere are the motions of these streamwise vortex pairs, rather than the dynamics of vorticity normal to the flow as in the case of cylinder VIV.

A compilation of peak amplitude response in the Griffin plot, as a function of the mass–damping, $(m^* + C_A)\zeta$, of the vibrating sphere, exhibits a good collapse of data, indicating a maximum saturated response of around 0.9 diameters, as mass–damping becomes extremely small. These results appear to be reasonably independent of the Reynolds numbers from 2000 to 12 000, and quite independent of the extent of streamwise vibrations of the tethered sphere. (One achieves a similar peak response, at a given mass–damping, even as the mass ratio, and therefore also the streamwise amplitude, are varied). This is quite different to the case of cylinder VIV (Jauvtis & Williamson 2004), where small increases in streamwise motion can change the mode of vibration and markedly increase the transverse vibration amplitude. It seems that the resulting effects of streamwise sphere motion on the streamwise vorticity and the transverse forces are less than for the cylinder VIV, where streamwise motion can distinctly change the formation of vorticity normal to the flow, and the resulting energy transfer to body vibration.

Following recent studies of cylinder VIV, we deduce the existence of a critical mass ratio, $m^*_{crit} \approx 0.6$, below which large-amplitude vibrations are predicted to persist to infinite normalized velocities. This might be compared with the discovery of such critical mass in other VIV systems: for example, for the transverse motion of a cylinder, $m^*_{crit} = 0.54$ has been found (Govardhan & Williamson 2000, 2002); for the two degree of freedom cylinder VIV in XY motion a value of 0.52 is found (Jauvtis & Williamson 2004); for the pivoted cylinder VIV a value of 0.5 is observed (Flemming & Williamson 2005).

An unexpected large-amplitude and highly periodic mode (mode III) is found at distinctly higher flow velocities where the frequency of vibration (f) is far below the frequency of vortex shedding for a static body (f_{vo}); i.e. $f \ll f_{vo}$. This has no apparent counterpart in the cylinder VIV case. The response amplitude plot is quite broad, extending continuously from $(U^*/f^*)S = 3$ to 8, and should not be confused with subharmonics. It appears that the low-frequency chain of streamwise vortex loops is able to impart lift (or transverse force) to the body, yielding a positive energy transfer per cycle, as indicated by our measurements of vortex force and displacement. This appears to be an example of the kind of vibration categorized by Naudascher & Rockwell (1994) in their book, as 'movement-induced vibration'. The sphere needs to move in the first place, in order to generate the self-sustaining mechanism of vortex-induced vibration. Without vibration of the body, there is no forcing at the sphere natural frequency to induce body motions.

Regarding further research concerning vibrating spheres, we are vigorously studying the wakes and dynamics of freely rising and falling spheres, and other bodies.

Preliminary results indicate strong similarities with the present study concerning tethered or elastically mounted bodies, under some conditions. One result stands out in particular; namely, the similarity of the mass where the unrestrained rising body suddenly starts to vibrate, which corresponds to the critical mass observed in the present work, both of which yield such a critical mass close to $m^*_{crit} = 0.6$.

The support from the Ocean Engineering Division of ONR, monitored by Dr Tom Swean, is gratefully acknowledged (ONR Contract Nos. N00014-04-1-0031 and N00014-95-1-0332). The authors thank also the wonderful help of the fluids FDRL lab group, especially Matthew Horowitz, Timothy Morse, Danny Broderick and Chris Atwell, and also the superb help of Chris Pelkie, of the Cornell Theory Center. Matt and Tim jumped in feet first to help this study often, and in particular, they enthusiastically made measurements of C_{EA} for the very light sphere included in this study. Many thanks, Matt and Tim, for this and other help!

REFERENCES

Anagnostopoulos, P. (Ed.) 2002 *Flow-Induced Vibrations in Engineering Practice*. WIT Press.

Batchelor, G. K. 1967 *An Introduction to Fluid Dynamics*. Cambridge University Press.

Bearman, P. W. 1984 Vortex shedding from oscillating bluff bodies. *Annu. Rev. Fluid Mech.* **16**, 195–222.

Bearman, P. W. & Currie, I. G. 1979 Pressure-fluctuation measurements on an oscillating circular cylinder. *J. Fluid Mech.* **91**, 661–677.

Blevins, R. D. 1990 *Flow-Induced Vibrations*. Van Nostrand Reinhold.

Brücker, C. 1999 Structure and dynamics of the wake of bubbles and its relevance for bubble interaction. *Phys. Fluids* **11**, 1781–1796.

Brücker, C. 2001 Spatio-temporal reconstruction of vortex dynamics in axisymmetric wakes. *J. Fluids Struct.* **15**, 543–554.

Carberry, J., Govardhan, R., Sheridan, J., Rockwell, D. & Williamson, C. H. K. 2003*a* Wake states and response branches of forced and freely oscillating cylinders. *Eur. J. Mech.* B **23**, 89–97.

Carberry, J., Ryan, K. & Sheridan, J. 2003*b* Experimental study of a tethered cylinder in a free stream. *Proc. IUTAM Symposium on Integrated Modeling of Fully Coupled Fluid-Structure Interactions Using Analysis, Computations, and Experiments,* 1–6 *June, New Brunswick, New Jersey, USA* (ed. H. Benaroya & T. Wei). Kluwer.

Carpenter, E. B., Leonard, J. W. & Yim, S. C. S. 1995 Experimental and numerical investigations of tethered spar and sphere buoys in irregular waves. *Ocean Engng* **22**, 765–784.

Feng, C. C. 1968 The measurements of vortex-induced effects in flow past a stationary and oscillating circular and D-section cylinders. Master's thesis, University of British Columbia, Vancouver, B. C., Canada.

Flemming, F. & Williamson, C. H. K. 2005 Vortex-induced vibrations of a pivoted cylinder. *J. Fluid Mech.* **522**, 215–252.

Gharib, M. R., Leonard, A., Gharib, M. & Roshko, A. 1998 The absence of lock-in and the role of mass ratio. In *Proce. Conference on Bluff Body Wakes and Vortex-Induced Vibrations, Washington, DC* (ed. P. W. Bearman & C. H. K. Williamson), Paper Number 24; also Paper FEDSM98-5312 in CD-ROM from ASME.

Govardhan, R. & Williamson, C. H. K. 1997 Vortex induced motions of a tethered sphere. *J. Wind Engng Ind. Aerodyn.* **69–71**, 375–385.

Govardhan, R. & Williamson, C. H. K. 2000 Modes of vortex formation and frequency response of a freely vibrating cylinder. *J. Fluid Mech.* **420**, 85–130.

Govardhan, R. & Williamson, C. H. K. 2002 Resonance forever: existence of a critical mass and an infinite regime of resonance in vortex-induced vibration. *J. Fluid Mech.* **473**, 147–166.

Griffin, O. M. & Ramberg, S. E. 1982 Some recent studies of vortex shedding with application to marine tubulars and risers. *ASME J. Energy Resour. Tech.* **104**, 2–13.

Griffin, O. M., Vandiver, J. K., Skop, R. A. & Meggitt, D. J. 1982 The strumming vibrations of marine cables. *Ocean Sci. Engng* **7**, 461–498.

Gu, W., Chyu, C. & Rockwell, D. 1994 Timing of vortex formation from an oscillating cylinder. *Phys. Fluids* **6**, 3677–3682.

Harleman, D. R. F. & Shapiro, W. C. 1961 The dynamics of a submerged moor sphere in oscillatory waves. *Coastal Engng* **2**, 746–765.

Horowitz, M. & Williamson, C. H. K. 2005 Vibrations of rising and falling spheres. *J. Fluid Mech.* In preparation.

Jauvtis, N., Govardhan, R. & Williamson, C. H. K. 2001 Multiple modes of vortex-induced vibration of a sphere. *J. Fluids Struct.* **15**, 555–563.

Jauvtis, N. & Williamson, C. H. K. 2003 Vortex-induced vibration of a cylinder with two degrees of freedom. *J. Fluids Struct.* **17**, 1035–1042.

Jauvtis, N. & Williamson, C. H. K. 2004 The effect of two degrees of freedom on vortex-induced vibration at low mass and damping. *J. Fluid Mech.* **509**, 23–62.

Jeon, D. & Gharib, M. 2001 On circular cylinders undergoing two-degree-of-freedom forced motions. *J. Fluids Struct.* **15**, 533–541.

Johnson, T. A. & Patel, V. C. 1999 Flow past a sphere upto a Reynolds number of 300. *J. Fluid Mech.* **378**, 19–70.

Khalak, A. & Williamson, C. H. K. 1996 Dynamics of a hydroelastic cylinder with very low mass and damping. *J. Fluids Struct.* **10**, 455–472.

Khalak, A. & Williamson, C. H. K. 1997 Fluid forces and dynamics of a hydroelastic structure with very low mass and damping. *J. Fluids Struct.* **11**, 973–982.

Khalak, A. & Williamson, C. H. K. 1999 Motions, forces and mode transitions in vortex-induced vibrations at low mass-damping. *J. Fluids Struct.* **13**, 813–851.

Koopmann, G. H. 1967 The vortex wakes of vibrating cylinders at low Reynolds numbers. *J. Fluid Mech.* **28**, 501–512.

Lamb, H. 1932 *Hydrodynamics*. Dover.

Leweke, T., Provansal, M., Ormières, D. & Lebescond, R. 1999 Vortex dynamics in the wake of a sphere. *Phys. Fluids* **11**, S12.

Leweke, T. & Williamson, C. H. K. 2004 Long-wavelength instability and reconnection of a vortex pair. *J. Fluid Mech.* (submitted).

Lighthill, J. 1986 Wave loading on offshore structures. *J. Fluid Mech.* **173**, 667–681.

Lin, J. C. & Rockwell, D. 1996 Force identification by vorticity fields: Techniques based on flow imaging. *J. Fluids Struct.* **10**, 663–668.

Magarvey, R. H. & Bishop, R. L. 1961 Transition ranges for three-dimensional wakes. *Can. J. Phys.* **39**, 1418–1422.

Milne-Thomson, L. M. 1973 *Theoretical Aerodynamics*. Dover.

Mittal, R. 1999 A Fourier-Chebyshev spectral collocation method for simulating flow past spheres and spheroids. *Intl J. Numer. Meth. Fluids* **30**, 921–937.

Moe, G. & Wu, Z.-J. 1990 The lift force on a cylinder vibrating in a current. *ASME J. Offshore Mech. Arctic Engng* **112**, 297–303.

Moreau, J. J. 1952 Bilan dynamique d'un écoulement rotationnel. *J. Math. Pure Appl.* **31**, 355–375.

Naudascher, E. & Rockwell, D. 1994 *Flow-Induced Vibrations: An Engineering Guide*. Balkema.

Ogihara, K. 1980 Theoretical analysis on the transverse motion of a buoy by a surface wave. *Appl. Ocean Res.* **2**, 51–56.

Ormières, D. & Provansal, M. 1999 Transition to turbulence in the wake of a sphere. *Phy. Rev. Lett.* **83**, 80–83.

Parkinson, G. 1989 Phenomena and modelling of flow-induced vibrations of bluff bodies. *Prog. in Aerospace Sci.* **26**, 169–224.

Perry, A. E., Lim, T. T. & Chong, M. S. 1980 The instantaneous velocity fields of coherent structures in coflowing jets and wakes. *J. Fluid Mech.* **101**, 243–256.

Provansal, M., Schouveiler, L. & Leweke, T. 1999 From the double vortex street behind a cylinder to the wake of a sphere. *Eur. J. Mech.* B *Fluids* **23**, 6580.

Saffman, P. G. 1992 *Vortex Dynamics*. Cambridge University Press.

Sakamoto, H. & Haniu, H. 1990 A study on vortex shedding from spheres in a uniform flow. *ASME J. Fluids Engng* **112**, 386–392.

Sarpkaya, T. 1979 Vortex-induced oscillations. *ASME J. Appl. Mech.* **46**, 241–258.

Sarpkaya, T. 1995 Hydrodynamic damping, flow-induced oscillations, and biharmonic response. *ASME J. Offshore Mech. Arctic Engng* **117**, 232–238.

Shi-Igai, H. & Kono, T. 1969 Study on vibration of submerged spheres caused by surface waves. *Coastal Engng Japan* **12**, 29–40.

Stanton, T. E. & Marshall, D. 1930 On the eddy system in the wake of flat circular plates in three dimensional flow. *ARC R & M* 1358.

Sumer, B. M. & Fredsøe, J. 1997 *Hydrodynamics around Cylindrical Structures.* World Scientific.

Tomboulides, A. G., Orszag, S. A. & Karniadakis, G. E. 1993 Direct and large-eddy simulations of axisymmetric wakes. *AIAA Paper* 93-0546.

Vethamony, P., Chandramohan, P. & Sastry, J. S. 1992 Estimation of added-mass and damping coefficients of a tethered spherical float using potential flow theory. *Ocean Engng* **19**, 427–436.

Williamson, C. H. K. & Govardhan, R. 1997 Dynamics and forcing of a tethered sphere in a fluid flow. *J. Fluids Struct* **11**, 293–305.

Williamson, C. H. K. & Govardhan, R. 2004 Vortex-induced vibrations. *Annu. Rev. Fluid Mech.* **36**, 413–455.

Williamson, C. H .K. & Roshko, A. 1988 Vortex formation in the wake of an oscillating cylinder. *J. Fluids Struct*. **2**, 355–381.